

Coherent X-ray Diffraction Microscopy

Stefano Marchesini and David Shapiro

September 23, 2008

Contents

1	Introduction	2
1.1	A Brief History of the Phase Problem	3
1.2	Scattering of X-rays by Homogeneous Media	7
1.2.1	The first Born approximation	7
1.2.2	The first Rytov approximation	9
1.3	Comparison of CXDM to other X-ray microscopes	10
2	Iterative Algorithms	11
2.1	General Formalism	11
2.2	Acceleration strategies	15
3	Experimental Design	16
3.1	Sampling and Transverse Coherence	17
3.2	Temporal Coherence	18
4	Data Acquisition and Pre-Reconstruction Analysis	18
4.1	Data Assembly	20
4.2	Pre-Reconstruction Diagnostics	22
5	Image Reconstruction	26
5.1	Image Averaging	26
5.2	Missing Data	30
5.3	Resolution analysis	32
5.4	Three-dimensional objects	34
6	Applications	34
6.1	Cell Biology	36
6.2	Materials Science	38
6.3	Hybrid Methods	40
6.4	Ultrafast Science	41
7	Conclusions	43
8	Acknowledgements	43

List of Figures

1	Bragg Sampling	4
2	First CXDM Demonstration	6
3	X-ray Penetration Depths	8
4	Scattering Geometry	9
5	Projection Operations	13
6	Hybrid Input-Output Behavior	14
7	Alternative fixed points	15
8	Basic experimental geometry	17
9	Data Acquisition Protocol	19
10	Diffraction from Yeast	21
11	Geometry of data acquisition	22
12	Three-dimensional diffraction data	23
13	Yeast autocorrelation	24
14	Spectrogram	25
15	Model reconstruction	27
16	PRTF	29
17	Vortex Modes	31
18	Unconstrained Modes	32
19	Variance Minimization	33
20	De-focus Effects	35
21	Diffraction imaging of E. Coli	36
22	High resolution imaging of yeast	37
23	High resolution imaging of nano-porous materials	38
24	Imaging strain fields in nano-crystals	39
25	Resonant diffraction imaging	40
26	Ultra-fast imaging with an FEL pulse	42

List of Tables

1	Summary of algorithms	12
2	Phase retrieval computational requirements	28

1 Introduction

In a normal microscope light scattered, reflected or emitted by an object forms a diffraction pattern which encodes information about the object's Fourier components. A lens recombines the scattered rays so that they interfere to form an image: it performs an inverse Fourier transform of the diffraction pattern to convert Fourier (reciprocal) representation of the object into a real space image.

At visible wavelengths, aberration-free lenses can provide diffraction (i.e. wavelength) limited images. X-rays are attractive for imaging for several reasons; they can provide much higher resolution images due to the short wavelength; their penetrating power offers the additional ability to

examine thick samples and their chemical sensitivity provides the prospect of elemental or molecular mapping. Unfortunately, X-rays are difficult to manipulate because fabricating suitable optics is a difficult technical challenge.

Diffraction and scattering experiments overcome this problem by eliminating optical elements. The scattering pattern created by an object is recorded on an area detector and the re-interference, which is normally done by a lens, is performed through numerical computation instead. Since no optical elements are needed, images may be obtained with resolutions limited in principle only by the maximum momentum transfer achieved.

The main problem with such lens-less schemes is the loss of the phase information in the measurement of the scattered light. When detecting diffraction patterns, only the intensity of the pattern is recorded; the phase-front information is lost. The intimate relationship between the phase-front and the direction of propagation of the light would seem to indicate that the task of recombining x-rays back at the sample position (or recovering unmeasured phases) was hopeless. Fortunately, if a small set of conditions are met, this is not so. In the 1980's several authors demonstrated that the solution to the phase retrieval problem is unique if the intensity is properly sampled [4, 8, 35, 48].

Coherent x-ray diffraction microscopy (CXDM) is an imaging scheme that extends the basic methodology of x-ray crystallography to non-crystalline samples. In other words, a sample is placed in an x-ray beam, the samples diffraction pattern is recorded on a segmented detector, the diffraction intensities are phased and then the structure of the sample is reconstructed by a Fourier transform. The fundamental difference lies in the nature of the sample, which directly results in an over-determined, and therefore simpler, inversion problem for CXDM. The CXDM sample is non-crystalline and isolated in space. When illuminated by a plane wave it creates a scattering pattern that is continuous though roughly broken up into regions of higher intensity called speckles. In contrast, the crystallographic diffraction pattern is concentrated into discrete peaks in reciprocal space because of the arrangement of many identical copies onto a regular grid. This lack of discrete peaks in the single particle case has two primary affects. First, the diffraction pattern is very weak and second it can be sampled on a finer interval than the crystallographic case (Figure 1). The weakness of the pattern implies that the very high intensities available at a third generation synchrotron undulator source will be needed to record data at large scattering angles and the fine sampling of the pattern is precisely what provides the missing phase information needed to reconstruct the object.

1.1 A Brief History of the Phase Problem

It was the realization by Bragg, in the first half of the 20th century, that the combination of appropriate phases with the recorded spots of a crystalline diffraction pattern would provide Fourier amplitudes, which set the course for crystallography throughout the rest of the century. The phases of the Fourier amplitudes are lost when scattered intensities are measured and the majority of theoretical development in crystallography has been aimed at methods of recovering that phase information. This is the phase problem. Since mother nature restricts us to only measuring intensities, all methods of phase retrieval rely on decoding phase information that has been encoded in intensity measurements. Crystallographers, and the subsequent diffraction microscopists, have two basic methods for doing this. The first, the holographic method, mixes a known reference signal with the desired and unknown signal. The coherent superposition of these two signals results in measureable intensity variations that are directly related to the relative phase. This is indirectly

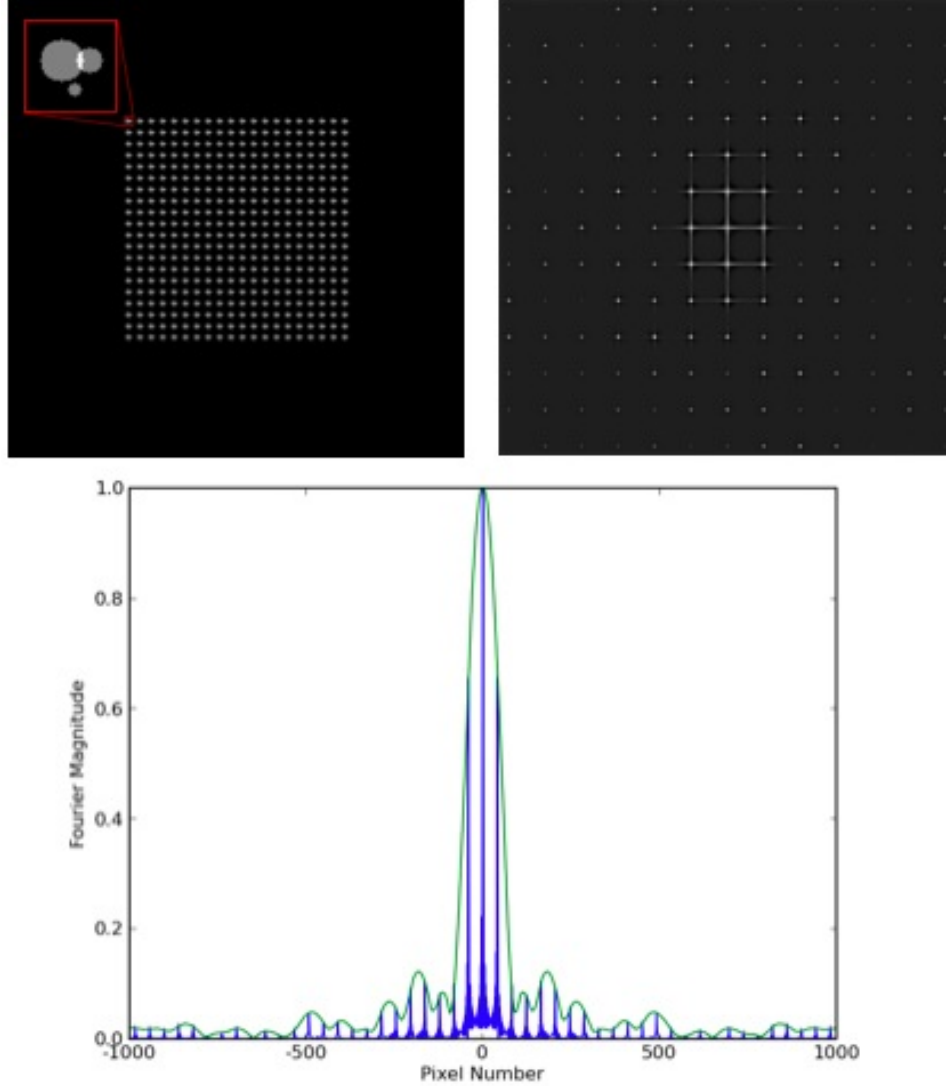


Figure 1: (a) Pseudo-crystal consisting of 20x20 unit cells. (b) Diffraction pattern calculated from (a). The diffraction intensity is concentrated into Bragg peaks though some intensity still exists between peaks because the crystal is of finite size. (c) Lineout through the center of (b) and the diffraction pattern calculated from a single unit cell from (a). Bragg peaks sample the single particle diffraction pattern but only at discrete locations.

a phase measuring method. The second method relies on only the signal from the unknown structure and additional information, supplied by the scientist, which is physically plausible. This is a constraint based method. Both methods seek to fill the information deficit inherent in intensity measurements by adding something that may unlock the phase.

Early in its development, crystallography relied primarily on the second, constraint based, method. Techniques that use Fourier refinement, the Patterson map, and direct methods all require the scientist to postulate some characteristic of the unknown structure. These postulates range from educated guesses at the atomic arrangement, as in Fourier refinement, to the requirement that the electron density be positive or localized to discrete atomic locations, as in direct methods. Advances in crystal growing techniques and, later on, the availability of modern synchrotron sources made possible the use of the holographic method. In the early 1950s it was discovered that heavy atoms could be added to large protein molecules without significantly altering the protein crystal structure. The strong scattering from the heavy atom would act as a reference signal for the holographic encoding of the desired phase information. Recording diffraction patterns from several crystals, each with a different isomorphous derivative, could allow for the recovery of the phases of the native protein structure. Though successful, this method requires the development of at least a few crystal derivatives. Multiple-wavelength anomalous diffraction phasing (MAD) requires only a single derivative. In this case, wavelengths are chosen to be near an absorption edge of the heavy-atom substructure. Additional structural information appears in the diffraction pattern when the Friedel symmetry is broken by anomalous dispersion. Today, this is the dominant method for protein crystallographers.

In 1980 David Sayre made the suggestion to treat an isolated non-crystalline sample as a crystallographer would treat a crystal [58]. That is, place it in a collimated and monochromatic x-ray beam and record its far-field diffraction pattern. At the time, the precise method of phasing the pattern was not clear but Sayre assumed that the holographic method should be possible by the placement of a known micro-fabricated object in the vicinity of the unknown sample. The known object would act as a phasing reference as implemented in modern Fourier transform holography (FTH). Up until this suggestion, and the advent of bright synchrotron x-ray sources, the FTH geometry required the use of a fresnel zone plate to focus the incident radiation to a small point in the plane of the object [55]. The cleaner approach of placing the sample plus fixed reference in a coherent x-ray beam could not be realized until several years later [10, 17, 59]. By this time, however, developments in other areas of physics would provide the key to solving the single-particle diffraction phase problem without the use of a reference object.

Algorithms being developed for electron microscopy in the early 1970s would establish the paradigm of iterative phase retrieval from Fourier modulus measurements [57]. In particular, the alternating projection algorithm of Gerchberg and Saxton, was developed to reconstruct the phase information that is missing when intensity measurements are made in both real and reciprocal space. This algorithm was later modified by Fienup into the input-output algorithm to handle cases where only one intensity measurement is made [30, 31, 33, 50]. The object domain constraints had to be modified to handle the lack of intensity measurements in that domain. In general, the only real space constraint needed is now known as finite support which restricts the object to an area that is no larger than half the width of its autocorrelation. The output of the Fourier modulus constraint is driven by its input which is calculated from the previous input using a feedback parameter. The combination of the input-output algorithm and the error reduction algorithm was found to be a very robust method of image reconstruction using only Fourier domain intensities but its success

was not understood for several years. In 1982, Bates argued that the solutions to the phase problem are unique in two dimensions if the Fourier modulus is sampled on an interval at least twice as fine as the Bragg interval [4, 5]. The method of phase retrieval from diffraction patterns sampled on this fine interval, the Nyquist interval, became known as the oversampling phasing method. The oversampling method compensates for the information deficit of missing phases by supplying a zero density region in the object domain. The finer the diffraction pattern is sampled the larger this zero density region is though this only adds useful information up to a certain point. This addition of information through Fourier space sampling results in an overdetermined inverse problem with a unique solution.

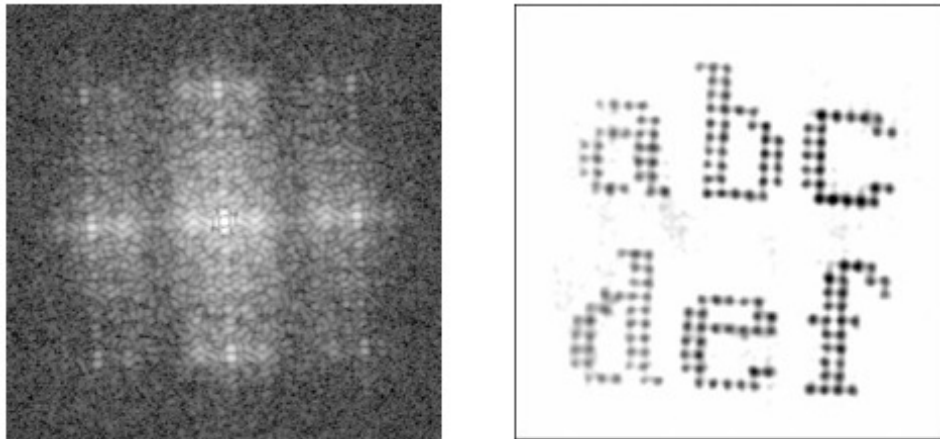


Figure 2: First soft x-ray demonstration of the CXDM method. (a) Diffraction pattern using 1.7 nm x-rays. (b) reconstruction of (a) to 75 nm resolution. (Reproduced from [49]).

Sayre claimed that the real niche of coherent x-ray diffraction microscopy (CXDM) would be imaging of few-micron objects at few nanometer resolution using soft x-rays (1-10 nm). The resolution and wavelength would scale up linearly from the crystallographic case but the sample size would scale down because of the increased interaction cross-section at the longer wavelengths. Thus CXDM would find wide application in the cell biology and materials sciences communities and fill the gap between the capabilities of electron microscopes and visible light microscopes. The CXDM method was first demonstrated in 1999 when Miao et al imaged a micro-fabricated test object using 1.7 nm x-rays. Indeed, the object was about $2\ \mu\text{m}$ in extent and was imaged to 75 nm resolution (Figure 2) [49].

In this case the resolution is limited by the scattering angle to which adequate signal is recorded. A dose of 10^6 Gy was delivered to the sample in a 15 minute exposure at beamline X1A of the National Synchrotron Light Source at Brookhaven National Laboratory. The brilliant x-ray beams of low emittance third generation synchrotron sources can deliver 100 times the dose in 1 tenth the time. This has made imaging at nearly 10 nm resolution possible with exposures of just a few tens of seconds. This very large dose required for high resolution imaging means that sensitive samples must be protected from the harmful effects of ionizing radiation. As will be discussed later, radiation damage is ultimately what limits the resolution of imaging unique radiation sensitive particles.

1.2 Scattering of X-rays by Homogeneous Media

In the soft x-ray region of the electromagnetic spectrum, the complex index of refraction can be written as:

$$\tilde{n} = \sqrt{\tilde{\epsilon}} = 1 - \frac{n_a r_e \lambda}{2\pi} (f_1 + i f_2) \quad (1)$$

where $f = f_1 + i f_2$ is the effective number of electrons and is calculated as a summation of complex scattering factors over allowed atomic transitions [42]. It is conventional to write $n = 1 - \delta - i\beta$ where δ and β have been tabulated for the atomic elements [36]. For wavelengths shorter than a few nm δ and β are positive and small. Thus the index of refraction in a continuous medium is slightly less than unity. Plane wave illumination, $\psi(z) = e^{-ik_0 z}$ becomes $\psi(z) = e^{-i\tilde{n}k_0 z}$ inside the material and therefore the intensity is:

$$I = |\psi(z)|^2 = I_0 e^{-2\beta k_0 z} = I_0 e^{-\mu z} \quad (2)$$

where μ is the absorption coefficient. Objects which have an overall thickness of less than about one attenuation length ($1/\mu$) can be considered optically thin or single scatterers. In the water window, Figure (4), this amounts to several microns for water and several hundred nanometers for protein. X-ray photons in this energy range are therefore ideally suited for coherent scattering from small biological specimens.

1.2.1 The first Born approximation

The wavefield scattered from such material must satisfy the inhomogenous Helmholtz wave equation [11]:

$$\nabla^2 \psi_s(\mathbf{r}) - k^2 \psi_s(\mathbf{r}) = k^2 O(\mathbf{r}) \psi(\mathbf{r}) \quad (3)$$

Here the total field, $\psi(\mathbf{r}) = \psi_i(\mathbf{r}) + \psi_s(\mathbf{r})$, is the incident plus the scattered field and $O(\mathbf{r})$ is the object scattering potential given by,

$$O(\mathbf{r}) = 1 - \frac{n^2(\mathbf{r})}{n_0} \simeq \frac{-2\delta n}{n_0}, \quad (4)$$

where $\delta n = \delta + i\beta$. The First Born Approximation, or weak scattering approximation, assumes that the scattered field is small compared to the incident field, i.e. that

$$|\psi_s(\mathbf{r})| \ll |\psi_i(\mathbf{r})|. \quad (5)$$

If this holds then the wave equation can be written as,

$$\nabla^2 \psi_s(\mathbf{r}) - k^2 \psi_s(\mathbf{r}) = -2k^2 \frac{-2\delta n}{n_0} \psi_i(\mathbf{r}) \quad (6)$$

and the approximate solution is given by the integral equation,

$$\psi_s(\mathbf{r}) = k^2 \int_V \psi_i(\mathbf{r}) O(\mathbf{r}) G(\mathbf{r} - \mathbf{r}') d\mathbf{r}' \quad (7)$$

where G is the outward propagating free-space Green's function. Using plane wave illumination and the far-field approximation, where $|\mathbf{r} - \mathbf{r}'| \simeq r - \mathbf{s} \cdot \mathbf{r}'$, the scattered wave becomes [7]

$$\psi_s(\mathbf{r}) = \frac{k^2 e^{ikr}}{r} \int_V O(\mathbf{r}) e^{ik(\mathbf{s} - \mathbf{s}_0) \cdot \mathbf{r}'} d\mathbf{r}'. \quad (8)$$

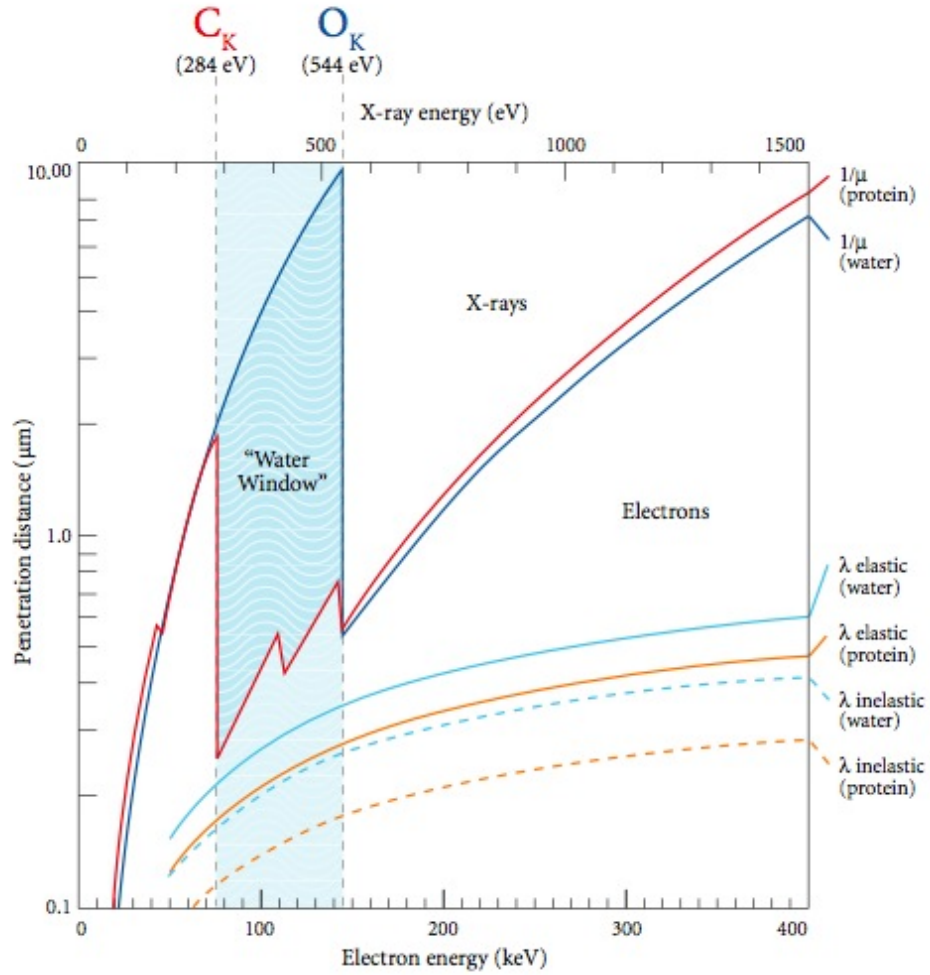


Figure 3: Penetration depth of x-rays and electrons in water and protein. Water window x-rays provide the highest contrast for hydrated biological material and can be used to image samples up to 10 microns thickness. Electrons are limited to specimens less than about 1 micron in thickness because of multiple scattering. (Reproduced from [45]).

\mathbf{s} and \mathbf{s}_0 are unit vectors in the direction of the incident wave propagation and the scattered field respectively. The source term in the inhomogeneous Helmholtz equation (incident free-space plane wave) is the zeroth order term in a perturbation expansion of the total field where we are only interested in solving for the first order term. Higher order scattering events are neglected. This basic result of the Born approximation shows that the scattered wave in the far-field is the Fourier transform of the scattering potential and, coupled with the relationship between finite support and oversampling, provides the foundation for the iterative phase retrieval process.

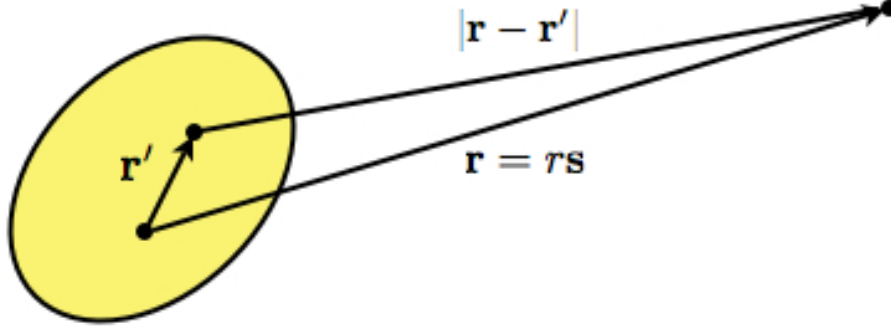


Figure 4: Geometry of the Born approximation. Waves scattered by points separated by \mathbf{r}' interfere and are observed in the far-field in the direction of $\mathbf{s} = \mathbf{q}/k$.

1.2.2 The first Rytov approximation

The validity of the Born approximation depends upon the wavelength and the optical thickness of the material. Efforts to theoretically characterize the validity domain of the approximation have produced different results that depend strongly on the particular application. A rough estimate that is in reasonable agreement with the rule of thumb of $t \leq 1/\mu$ requires that [11]

$$k \frac{|\delta n|}{n_0} t \ll 1 \quad (9)$$

The basic assumption of the Rytov expansion is that the perturbation is multiplicative instead of additive as in the Born approximation. The multiplicative term is conveniently taken to be exponential so that zero perturbation returns the free-space field according to,

$$\psi_{Rytov} = \psi_i e^{\phi} \quad (10)$$

where the argument of the exponential is now expanded as

$$\phi = \epsilon\phi_1 + \epsilon\phi_2 + \dots \quad (11)$$

The laplacian of the first order term again gives the inhomogeneous helmholtz equation

$$\nabla^2(\psi_i \phi_1) + k^2(\psi_i \phi_1) = -2k^2 \delta n \psi_i \quad (12)$$

which is the same as the Born approximation with $\psi_s = \psi_i \phi_1$. The scattered field is then

$$\psi_{Rytov} = \psi_i e^{\psi_s/\psi_i} \quad (13)$$

where ψ_s is the scattered field in the first order Born approximation. The first term in an expansion of the Rytov field is the Born approximation and so the Rytov approximation is considered to account for higher order effects and cover longer propagation distances. Unfortunately, there is not a linear relationship between this field and the scattering potential as with the Born field. As will be discussed later, the full three-dimensional reciprocal space of an object is measured by recording the two-dimensional scattered wavefield at many angular orientations of the object. These diffraction patterns are then mapped onto a regular 3D grid for reconstruction. This is not possible if the Born approximation does not apply because of the breakdown of that linear relationship. Two-dimensional reconstructions are still feasible but they represent the structure of the x-ray wavefield after complete propagation through the object.

1.3 Comparison of CXDM to other X-ray microscopes

Every imaging system has benefits and drawbacks. The key benefits of diffraction imaging are the simplicity of the experimental arrangement, the achievable resolution, the efficiency and the ability to image in phase contrast and absorption contrast simultaneously without the addition of special optical elements. The basic CXDM setup requires only a coherent x-ray beam, an aperture suitable for coherence selection, a beamstop, and a segmented detector. Since translations of the sample do not effect the diffraction pattern, due to the Fourier shift theorem, vibrational amplitudes nearly as large as the sample itself are tolerable. This assumes that the illumination field is flat and significantly broader than the specimen. If this holds, then almost no precautions need to be taken to mechanically stabilize the experimental apparatus. This is in stark contrast to the laser interferometer systems needed to maintain the relative positions of sample and zone plate in modern scanning transmission x-ray microscopes. The main limitation of lens based microscopes, both full-field and scanning transmission microscopes, is in fact the lenses. The diffractive optics, zone plates, used by most x-ray imaging systems have a very low numerical aperture and the imaging resolution is ultimately limited by the smallest feature present in the grating, the outer most zone width. This is a technological hurdle which has the state-of-the-art lenses producing 15-30 nm resolution images in two dimensions. Undoubtedly, incremental improvements will push this resolution into the sub-10 nm region but, as a general rule of thumb for all types of imaging, as the resolution improves the sample size must shrink. For zone plates, this is due to the relationship between depth-of-focus and outer most zone width,

$$D_{focus} = \frac{2\Delta r^2}{\lambda} \quad (14)$$

A zone plate capable of 15 nm resolution using water window x-rays will have a depth of focus of only a few hundred nm. A further experimental complication is that this same zone will have a focal length on the order of 500 microns. These two quantities combined make three-dimensional imaging of thick objects very difficult at high resolution. They can be alleviated somewhat by going to higher energies but the incident flux required for imaging scales roughly as λ^{-2} indicating that brighter sources are needed while the efficiency of high energy zone plates also suffers because of the difficulty in making thick but narrow zones [23]. Furthermore, the roll-off of the modulation

transfer function at high spatial frequencies also leads to high imaging doses. The total efficiency for diffractive optics is in the neighborhood of 10% however it can be significantly lower at the highest spatial frequency.

Though the efficiency of CXDM is roughly equivalent to the quantum efficiency of the CCD detector, 90%, and the resolution is only limited by photon statistics at the largest scattering angles recorded, currently around 5-10 nm, there is an enormous computational cost. With improved detectors and sources it is reasonable to expect 3D imaging of radiation hard samples of a few microns in size to 2-3 nm resolution. This, however, requires the measurement and subsequent optimization of 1 billion resolution elements. This is an enormous task that is addressed in the next section. Furthermore, the process of measuring diffraction patterns gives the user very little feedback concerning the quality of the specimen. This requires preparation of ideal specimens ahead of time which can be very difficult for disciplines such as cell biology. These limitations tend to greatly reduce the imaging throughput, though, when success is had the results can be stunning.

2 Iterative Algorithms

The computational problem of coherent diffractive imaging is stated as follows. An object of density or composition $\rho(\mathbf{r})$ is illuminated by a monochromatic plane wave which first propagates through the material and then through free-space to the detector. Light propagates through a linear transformation \mathcal{F} (typically a Fourier transform and a normalization factor) to the data space where we record an intensity pattern $I(\mathbf{k})$:

$$I(\mathbf{k}) = |\mathcal{F}\rho(\mathbf{r})|^2.$$

The aim is to recover the density or composition $\rho(\mathbf{r})$ as a function of the *real*(or *object*) coordinate \mathbf{r} from these measurements $I(\mathbf{k})$ and a set of constraints on the values that the object ρ can assume.

The requirement that the image fits the data and that it satisfies certain constraints can be met by simple computational operations. Propagation between the Fourier data domain and the “real” space - where the constraints are defined - is performed by Fourier transformations, thus these algorithms are sometimes referred to as “iterative transform algorithms”, even though Fourier transform are not strictly necessary (but offer greater speed).

2.1 General Formalism

Formally one can express the object and data space in terms of different bases ($\langle \mathbf{r} |$, $\langle \mathbf{k} |$), and define the transformation \mathcal{F} between them:

$$\rho(\mathbf{r}) = \langle \mathbf{r} | \rho \rangle \tag{15}$$

$$\tilde{\rho}(\mathbf{k}) = \langle \mathbf{k} | \rho \rangle \tag{16}$$

$$\mathcal{F}\rho(\mathbf{r}) = \tilde{\rho}(\mathbf{k}) = \sum_{\mathbf{r}} \langle \mathbf{k} | \mathbf{r} \rangle \langle \mathbf{r} | \rho \rangle \tag{17}$$

The projector operators can be defined in either basis, using whichever is more convenient (see Fig. 5).

To solve the phase problem in diffraction microscopy, one uses the fact that the object being imaged is of finite extent, limited by a support mask S . Diffraction microscopy requires an algorithm

Algorithm	Iteration $\rho^{(n+1)} =$
ER	$\mathbf{P}_s \mathbf{P}_m \rho^{(n)}$
SF	$\mathbf{R}_s \mathbf{P}_m \rho^{(n)}$
HIO	$\begin{cases} \mathbf{P}_m \rho^{(n)}(\mathbf{r}) & \mathbf{r} \in S \\ (\mathbf{I} - \beta \mathbf{P}_m) \rho^{(n)}(\mathbf{r}) & \mathbf{r} \notin S \end{cases}$
DM	$\{\mathbf{I} + \beta \mathbf{P}_s \{[(1 + \gamma_s) \mathbf{P}_m - \gamma_s \mathbf{I}] - \beta \mathbf{P}_m [(1 + \gamma_m) \mathbf{P}_s - \gamma_m \mathbf{I}]\} \rho^{(n)}$
ASR	$\frac{1}{2} [\mathbf{R}_s \mathbf{R}_m + \mathbf{I}] \rho^{(n)}$
HPR	$\frac{1}{2} [\mathbf{R}_s (\mathbf{R}_m + (\beta - 1) \mathbf{P}_m) + \mathbf{I} + (1 - \beta) \mathbf{P}_m] \rho^{(n)}$
RAAR	$[\frac{1}{2} \beta (\mathbf{R}_s \mathbf{R}_m + \mathbf{I}) + (1 - \beta) \mathbf{P}_m] \rho^{(n)}$

Table 1: Summary of various algorithms

that can solve the following non-convex optimization problem:

$$\min_{\tilde{\rho}} \left\| |\tilde{\rho}(\mathbf{k})| - \sqrt{I(\mathbf{k})} \right\|^2, \text{ subject to } \rho(\mathbf{r}) = 0 \text{ if } \mathbf{r} \notin S.$$

where the Euclidean norm $\left\| |\tilde{\rho}| - \sqrt{I} \right\|^2$ is invariant with respect to a Fourier transform.

Alternating projection methods for closed convex sets date back to von Neumann [52]. The first recognized application of these algorithms to the phase retrieval problem was described by Gerchberg and Saxton [57]. In 1982 Fienup showed how these alternating projections methods are equivalent to the gradient descent method (“error reduction”), of constrained optimization [31].

Using the Euclidian norm (Fig. 5) to quantify the violation of the support mask constraint:

$$\varepsilon_s^2(\rho) = \|\rho - S\rho\|^2 = \|[\mathbf{I} - \mathbf{P}_s]\rho\|^2, \quad (18)$$

one can define the corresponding projector ($\mathbf{P}_s \rho(\mathbf{r}) = \{\rho(\mathbf{r}) \text{ if } \mathbf{r} \in S; 0 \text{ otherwise}\}$) that acts element-by-element on the real space basis. To quantify the discrepancy with the Fourier data we use again the Euclidean norm, and a projector operator that defines a similar relation to the error metric ε_m :

$$\varepsilon_m^2(\rho) = \left\| |\mathcal{F}\rho| - \sqrt{I} \right\|^2 = \|[\mathbf{I} - \mathbf{P}_m]\rho\|^2. \quad (19)$$

To compute the projector corresponding to the Fourier magnitude constraint, one first needs to propagate ρ to the data space by a Fourier transform, then replace estimated magnitudes $|\tilde{\rho}|$ with the measured ones, \sqrt{I} , and finally propagate back to real space. Using these transforms one simplifies the calculation of the projection which becomes an element-wise operation on each recovered Fourier component. Formally, the forward \mathcal{F} and inverse \mathcal{F}^{-1} Fourier transforms must be incorporated into the operator defined in real space \mathbf{P}_m :

$$\mathbf{P}_m = \mathcal{F}^{-1} \tilde{\mathbf{P}}_m \mathcal{F}, \quad (20)$$

where the measured fourier magnitudes are enforced in Fourier space by $\tilde{\mathbf{P}}_m$. Using the Fourier basis, one simply replaces the estimated magnitudes $|\tilde{\rho}|$ with the measured ones \sqrt{I} , ($\tilde{\mathbf{P}}_m \tilde{\rho}(\mathbf{k}) = \sqrt{I(\mathbf{k})} \frac{\tilde{\rho}(\mathbf{k})}{|\tilde{\rho}(\mathbf{k})|}$), as described in Fig 5.

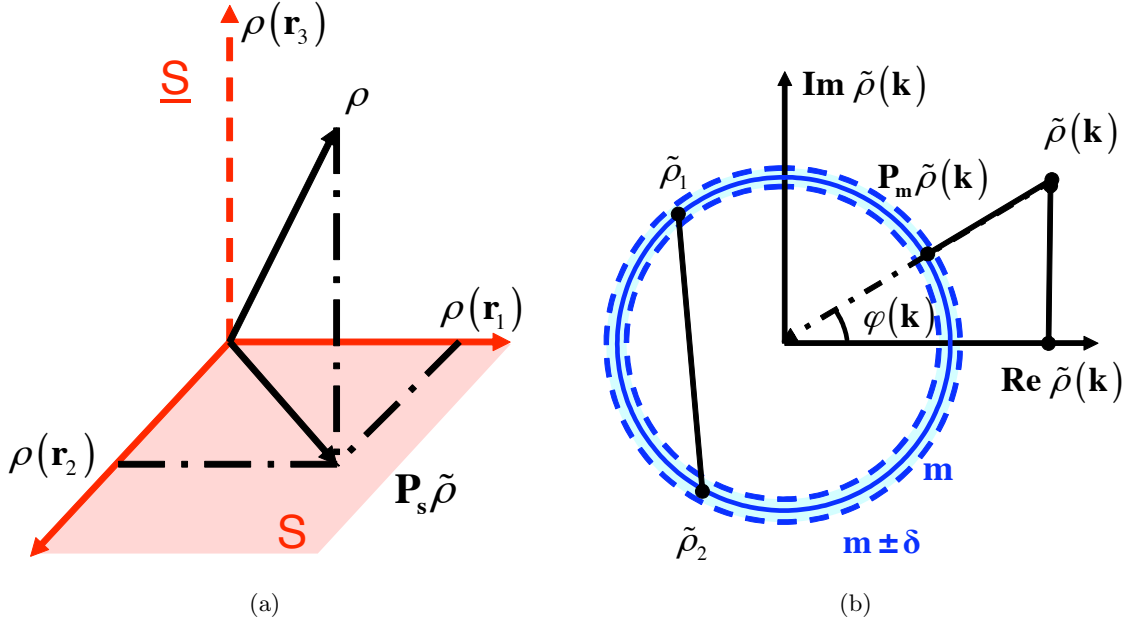


Figure 5: (a) Three pixel values on cartesian axes. The projection on the support set S is performed simply by setting to 0 all the pixels outside the support mask ($\mathbf{P}_s \rho(\mathbf{r}) = \{\rho(\mathbf{r}) \text{ if } \mathbf{r} \in S; 0 \text{ otherwise, i.e. } \mathbf{r} \in \underline{S}\}$). The length (in euclidean terms) of the projection step ($[\mathbf{P}_s - \mathbf{I}]\rho$) represents the distance from the constraints $\varepsilon_s^2(\rho)$. (b) To compute the projector corresponding to the Fourier magnitude constraint, one enforces that the image fourier magnitudes are equal to the measured ones, by simply replacing estimated magnitudes with measured ones, leaving the phase unchanged. The projection operation is performed element-wise (at each data point \mathbf{k}): $\tilde{\mathbf{P}}_m \tilde{\rho}(\mathbf{k}) = \sqrt{I(\mathbf{k})} \frac{\tilde{\rho}(\mathbf{k})}{|\tilde{\rho}(\mathbf{k})|}$. The length of projecting steps represents the distance from the estimate to the measured data set, which defines the discrepancy with the data $\varepsilon_m^2(\rho)$. The problem here lies in the fact that from the center of the circle the projection is undefined, we do not know which phase to apply to the Fourier amplitude. The non-convexity of this operation causes standard methods to fail.

The convergence properties of projection methods are well established for convex problems. The projector operators are related to the gradients of the errors to be minimized as:

$$[\mathbf{I} - \mathbf{P}_m]\rho = \frac{1}{2}\nabla_{\rho}\varepsilon_m^2(\rho), \quad (21)$$

$$[\mathbf{I} - \mathbf{P}_s]\rho = \frac{1}{2}\nabla_{\rho}\varepsilon_s^2(\rho) \quad (22)$$

The original alternating projection method applies successive iterations of the form:

$$\rho^{(n+1)} = \mathbf{P}_s \mathbf{P}_m \rho^{(n)} = \mathbf{P}_s \rho^{(n)} - \frac{1}{2}\mathbf{P}_s \nabla \varepsilon_m^2(\rho^{(n)}), \quad (23)$$

and thus the fit to the data, ε_m^2 , is performed without ever leaving a constraint set, moving along the direction of steepest descent. Despite the convergence properties of alternating projection, and similar error reduction methods, they are not suited to solve nonconvex problems, which require strategies to search beyond local minima (see Fig 6).

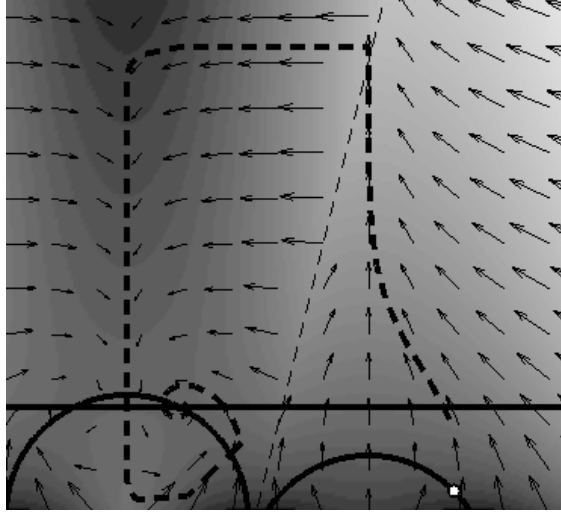


Figure 6: The Hybrid Input Output algorithm (dashed curve) is capable of escaping a local minima. The first constraint (support) is depicted by a horizontal line, while the other constraint is depicted by two circles. If the first guess is near a local minimum, the algorithm moves away from it, in the direction of the gap until it finds the other attractor to one of the true solutions, the intersection of the two sets. Arrows indicate the direction toward the fixed point defined by the differential version of the HIO algorithm. The differential version seeks the saddle point of the map represented in the background in grayscale. See also Figfig:fixed points.

Over the past 30 years, a number of algorithms using recursive operations formed by combining projection operators in different ways have been proposed (table 1). The fixed points of projection algorithms are defined in terms of a recursive solution to a succession of projection operators. The combination of operators is formed in such a way that the algorithm stops at a fixed point which is related, but not necessarily equal to the solution that satisfies both constraints simultaneously.

One of the most successful examples of projection algorithms is Fienup's Hybrid Input-Output (HIO) method, originally derived using ideas from nonlinear control feedback theory [31]. The operation of enforcing the measured Fourier magnitudes is considered as a nonlinear black box, and we seek to stabilize the response of this box. The key to the success of the HIO algorithm was to mix and match the input and the output, inside and outside the support mask. This heuristic algorithm does not necessarily decrease the distance to the constraints, but moves toward a condition of equilibrium from a much larger area of convergence. The best estimate of the unknown object is obtained after enforcing measured Fourier magnitudes.

V. Elser extended the HIO algorithm further. By tuning an adjustable parameter his difference map varies between the original HIO algorithm, its counterpart obtained by swapping projection operators, and combinations thereof. A number of applications of this algorithm have been demonstrated [18, 24, 27, 64]. The additional parameter allows for greater flexibility of the difference map algorithm, but comes at a cost. It adds more parameters to tune and requires greater computational effort for each iteration. The RAAR method developed by R. Luke is a compromise between the ability of these algorithms to wander around in search of better solutions, and more standard local optimization methods [14]. The choice between these algorithms is a matter of heuristic taste.

The convergence dynamics of these algorithms exhibit the behavior typical of a chaotic system,

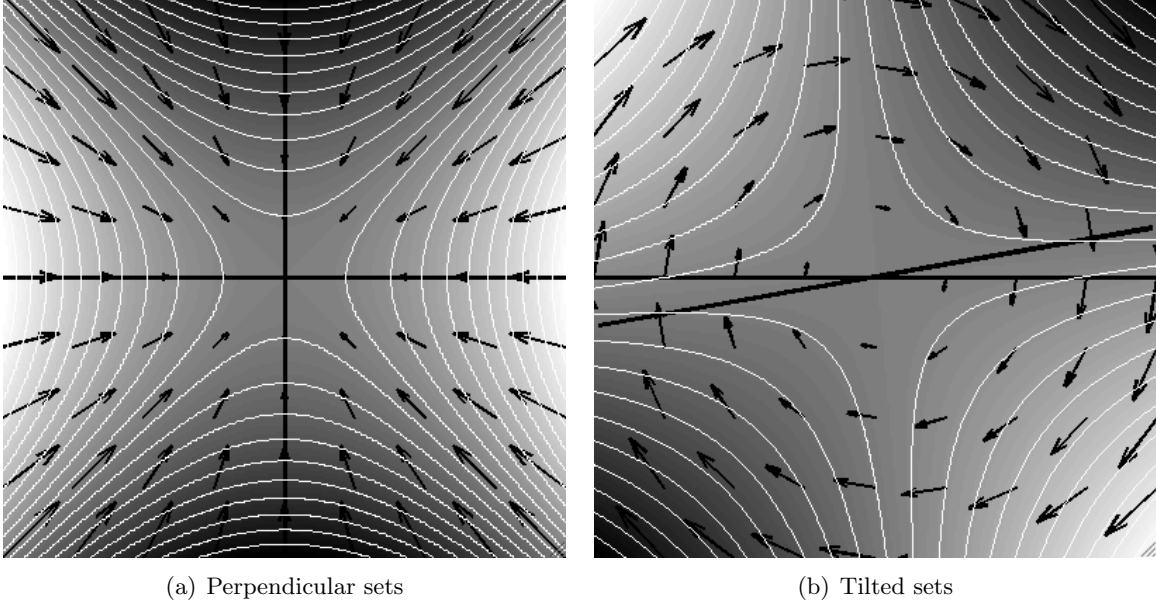


Figure 7: Alternative fixed point used by the Hybrid Input Output algorithm. Imagine that we seek the intersection of two lines, $x = 0$ and $y = 0$ starting from a point \mathbf{r} . We could simply define our function $\varepsilon(\mathbf{r}) = x^2 + y^2$ and minimize it, by standard optimization algorithms. But, as shown in (a), we would reach the same solution using the hyperbolic function $\mathcal{L}(\mathbf{r}) = x^2 - y^2$, and moving toward the intersection $\min_x \max_y \mathcal{L}$. To do this one moves in the direction $(-\partial_x \mathcal{L}, \partial_y \mathcal{L})$ (indicated by arrows in the figures). The twist, shown in (b), comes when we replace \max_y with $\max_{\text{not } x}$, where “not x ” means any parameter except for x . If the axis y is not perpendicular to x , the behavior of the fixed point changes dramatically, and leads to a spiralling orbit toward the attractive fixed point. When the two constraints are parallel, such as near a local minimum, the algorithm moves away, in the direction of their gap.

sometimes converging in a few iterations, sometimes after thousands. Such chaotic behavior is probably the price to pay for allowing the algorithm to find its fixed point from a larger region of the solution space than standard local optimization methods. By remaining true to the data however, projection algorithms seem to outperform purely stochastic methods. Optimizing the step length appears to further improve rapidity and reliability of convergence within a limited number of iterations.

2.2 Acceleration strategies

Like a gradient or sub-gradient method, alternating projections can be slow. Acceleration can be obtained by adjusting the step length, adding a one dimensional search at each iteration. One adjusts a multiplication factor δ to the step $\Delta\rho = -\frac{1}{2}\nabla_s \varepsilon_m^2(\rho)$ until we have reached a minimum. Once we identify the direction to search by a projection operation:

$$\Delta\rho_s = \mathbf{P}_s[I - \mathbf{P}_m]\rho$$

one increases the step by a multiplicative factor δ until a minimum of ε_m^2 is reached such that:

$$\frac{\partial}{\partial \delta} \varepsilon_m^2(\rho + \delta \Delta\rho) = \langle \Delta\rho | \nabla \varepsilon_m^2(\rho + \delta \Delta\rho) \rangle_r = 0.$$

At the minimum value \mathbf{r}' , the new gradient is uncorrelated with the step direction, successive search directions become perpendicular. Use of conjugate directions and other acceleration strategies can further speed up convergence.

Efforts to speed up HIO-type algorithms for nonconvex problems have been successfully demonstrated [47]. The HIO algorithm described in differential form, seeks the solution to the following saddle-point problem (Fig. 7):

$$\min_{\rho_s} \max_{\rho_{\underline{s}}} \mathcal{L}(\rho_s + \rho_{\underline{s}}) \quad (24)$$

$$\mathcal{L}(\rho_s + \rho_{\underline{s}}) = \varepsilon_m^2(\rho_s + \rho_{\underline{s}}) - \varepsilon_s^2(\rho_s + \rho_{\underline{s}}), \quad (25)$$

where $\rho_s = \mathbf{P}_s \rho$ and $\rho_{\underline{s}} = \mathbf{P}_{\underline{s}} \rho = [\mathbf{I} - \mathbf{P}_s] \rho$. The step $\Delta \rho$ used in HIO (table 1) can be expressed in terms of this gradient $\nabla \mathcal{L}$:

$$\begin{aligned} \Delta \rho &= \rho^{(n+1)} - \rho^{(n)} \\ &= \{\mathbf{P}_s[\mathbf{P}_m - \mathbf{I}] - \beta \mathbf{P}_{\underline{s}} \mathbf{P}_m\} \rho, \\ &= \{-\mathbf{P}_s + \beta \mathbf{P}_{\underline{s}}\} \frac{1}{2} \nabla \mathcal{L}(\rho). \end{aligned} \quad (26)$$

The adjustment of this step length is equivalent to adjusting the feedback parameters on the fly by applying a lower dimensional optimization to each step. Further gains can be made through optimization of the steps in both the descent and ascent directions by solving:

$$\min_{\alpha} \max_{\beta} \mathcal{L}(\rho_s - \alpha \frac{1}{2} \nabla_s \mathcal{L}(\rho), \rho_{\underline{s}} - \beta \frac{1}{2} \nabla_{\underline{s}} \mathcal{L}(\rho)) \quad (27)$$

When the step length is optimized in this way, successive iterations stop repeating the same search directions. The step directions of neighboring iterates become orthogonal.

3 Experimental Design

Synchrotron Radiation (SR) has been widely used since the 80's as a tool for many applications of UV [3], soft X rays and hard X rays in condensed matter physics, chemistry, biology, etc [1,12,29,46]. The evolution of SR sources towards higher brightness has led to the design of low-emittance electron storage rings (emittance is the product of beam size and divergence), and the development of special source magnetic structures, as undulators. This means that more and more photons are available in a narrow bandwidth and in a small collimated beam; in other words there is the possibility of getting a high power in a coherent beam. In most applications, a monochromator is used, and the temporal coherence of the light is given by the monochromator bandwidth.

With smaller and smaller sources, even without the use of collimators, the spatial coherence of the light has become appreciable, first in the UV and soft X ray range, and then also with hard X rays. This has made possible new or improved experiments in interferometry, microscopy, holography, correlation spectroscopy, etc. [29]. The basic experimental CXDM geometry is shown in Figure 8. There are several key tradeoffs when designing a basic coherent diffraction experiment. The obvious goal is to achieve the highest resolution possible, which requires an experimental geometry offering detection of very large scattering angles. The simple solution to this is to move the detector as close to the sample as possible since the achievable resolution is proportional to the scattering angle of the detector. Unfortunately, this also increases the solid angle of each individual

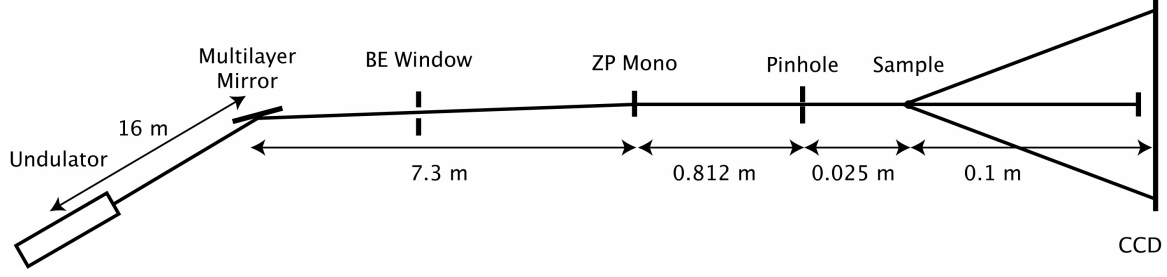


Figure 8:

detector pixel which in turn decreases the sampling interval of the diffraction pattern. Therefore, in order to have an optimized diffraction microscope, it is important to fully understand the sampling and coherence requirements of diffraction microscopy.

3.1 Sampling and Transverse Coherence

In the ideal case, a monochromatic plane wave illuminates a sample of width W , and the diffracted light is detected far downstream (in the far-field). Under far-field (Fraunhofer) conditions, the measured pattern corresponds to the Fourier transform *intensity* of the exit wavefield. The limited (discrete) sampling points from an area detector need to record sufficient information to enable the recovery of the entire object. The highest frequency fringes to be sampled will come from interference between rays coming from the edges of the object with the largest separation. If this separation is W , then the frequency of these fringes in the detector plane will be $W/z\lambda$, where λ is the illuminating wavelength and z is the distance between scattering object and detector plane.

The Nyquist-Shannon sampling theorem states that, given a band-limited signal that is uniformly sampled at a sufficient rate, even if all of the information in the signal between samples is discarded, there remains sufficient information that the original signal can be mathematically reconstructed perfectly from only those discrete samples. The intensity pattern is band-limited because its Fourier transform is the autocorrelation of the sample. For a sample of width W , the autocorrelation has width $2W$. The object must be perfectly isolated from any other scattering material. Using finite width illumination to define the isolated object does not work well in practice because producing such illumination with no tails has so far been in-practical.

Shannon's sampling theorem not only allows to reduce the number of detector pixels to a finite number, but relaxes other experimental requirements. A single monochromatic plane wave is no longer required for a finite sampling interval: measurements using superpositions of different plane waves may provide the same information at a fraction of the time. We can increase the number of incident photons on the sample as long as the angular divergence of the incoming waves does not significantly smear out the diffraction pattern,

Following Spence et al. [40], it seems reasonable to require that the angular spread of the beam be less than half that of the Shannon angle,

$$\Delta\theta \leq \frac{\Delta\theta_s}{2} \leq \frac{\lambda}{4W} \quad (28)$$

This is identical to the spatial coherence condition for partially coherent light that has been filtered with an aperture that is equal in size to our field of view, $2W$. Clearly it is not necessary to

illuminate the entire field of view since the empty region surrounding the object cannot contribute to the scattered intensity. However, it is necessary that the coherence length of the illumination be as big as the field of view, twice the object size. A formal treatment of partially coherent beam illumination utilizes the *mutual coherence function* of statistical optics. The mutual coherence function is the ensemble average of all the possible fluctuations of the phases contributing to the final measurement. The Schell theorem states that the diffracted intensity pattern of a static object illuminated by partially coherent light is the Fourier transform of the object's autocorrelation multiplied by the normalized mutual coherence function [2, 44]. The normalized mutual coherence, also known as *degree of coherence* is 1 for a fully coherent beam, and 0 for an incoherent one. Since the degree of coherence is a normalized quantity it can be larger than the beam itself. For an object of width W , the full width of the degree of coherence needs to be larger than $2W$. This does not imply that the beam profile needs to be twice the size of the sample. In addition, the finite sampling theory described above assumes point-like pixels. In reality, area detectors integrate over a pixel of the same size as the sampling rate, which has the same effect as using an incoherent source with the same angular dispersion as the solid angle attained by one pixel.

3.2 Temporal Coherence

One must also consider coherence in the longitudinal or temporal dimensions. The lack of full longitudinal coherence means that as two wave trains propagate they will go from a state of complete overlap to a state of zero overlap over a distance equal to the longitudinal coherence length. This distance is equal to half the wavelength and corresponds to a 180-degree phase shift that will result in destructive interference. Again, if we consider the worst case to be a 50% overlap of wavetrains than our longitudinal coherence length requirement becomes:

$$\frac{\lambda^2}{\Delta\lambda} = 2w\theta \quad (29)$$

where $w\theta$ is the greatest path difference between two rays originating at opposite edges of the sample of width w and arriving at the detector with maximum scattering angle θ . The half angle of the segmented detector is $N\Delta\theta/2$ so we can write:

$$\frac{\lambda}{\Delta\lambda} \geq \frac{wN\Delta\theta_s}{\lambda} = \frac{N}{2} \quad (30)$$

where we have noted that the Shannon angular interval is $\lambda/2W$. This relationship should not be understood as a limitation placed on the level of oversampling appropriate for a given spectral resolution. Rather, it is a practical consideration that indicates the size of detector you will need for critical sampling of a diffraction pattern recorded to the maximum resolution attainable with a given spectral resolution. The level of oversampling can always be increased by either using a detector with smaller pixels or by placing the detector further away from the sample.

4 Data Acquisition and Pre-Reconstruction Analysis

Coherent diffraction patterns of non-crystalline particles have a very large dynamic range because of the strong dependence of the scattered intensity on spatial frequency. It has been shown both theoretically and experimentally that the scattered intensity goes as f^{-4} [16, 23]. This, combined

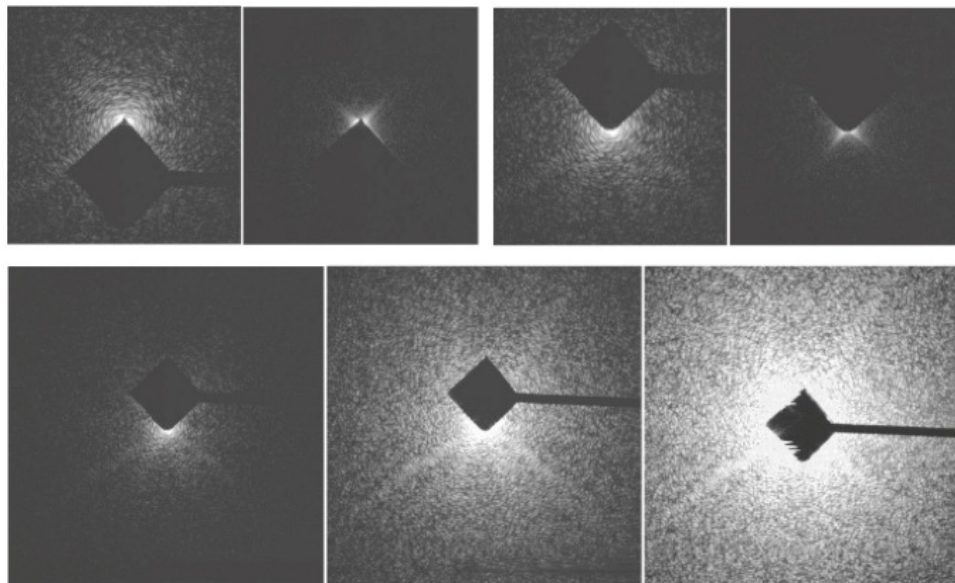


Figure 9: Acquisition of a single particle diffraction pattern. Top row: corner/beamstop are positioned at opposing corners for collection of complete pattern. Bottom row: different exposure times are needed to collect full dynamic range. The exposure times shown are 0.1, 1.0, and 10.0 seconds (Reproduced from [13])

with the low dynamic range and sensitivity to ionizing radiation of charge-coupled device detectors, places strict limitations on how diffraction data are collected. A typical CXDM diffraction pattern will contain spatial frequencies ranging from 0.001 nm^{-1} to 0.1 nm^{-1} and thus span at least four decades of intensity though commercially available CCDs can only record on the order of 1000 photons per pixel per acquisition. Further complicating this is the fact that radiation damage to the chip, though not fully understood, depends on the total dose delivered. Thus exposing the sample longer in order to get high spatial frequency information can shorten the lifetime of the detector if precautions are not taken to protect pixels at small scattering angles from over exposure. The usual solution to this problem is to use a combination of beamstops with different sizes. Small beamstops will block only the direct, unscattered, x-ray beam and the very brightest speckles of the specimens diffraction pattern during very short exposures. A larger beamstop can then be used for the longest exposures which will block much of the low angle portion of the diffraction pattern thereby protecting the sensitive detector.

The beam defining pinhole, consisting of sharp metallic edges, scatters a great deal of radiation in the area around the specimen of interest. If these photons are not blocked they will overwhelm the very weak specimen diffraction in the CCD recording. To this end, a secondary aperture with soft edges is placed immediately upstream of the sample. This *corner* aperture is a square many times larger than the beam defining pinhole and is positioned so that the x-ray beam is located in one corner. Thus only two edges at a time see bright x-radiation which is scattered predominantly in the direction of the aperture. This leaves three quadrants of clean diffraction data for collection simultaneously. The corner aperture is relocated to the opposing corner for collection of the final quadrant of data. Light leakage through this large secondary aperture is blocked by a beamstop whose shape and size match the shadow of the aperture in the plane of the CCD detector. Figure 9

describes the basic data acquisition process. A full diffraction dataset is a combination of dozens of individual CCD recordings that are combined during post processing. The exposure times range from milliseconds to perhaps hundreds of seconds, depending on the size and scattering strength of the specimen.

4.1 Data Assembly

The basic merging process is comprised of three steps: thresholding, masking, and averaging. The thresholding is performed at both the high end of the intensity scale, to remove saturated pixels and those pixels neighboring saturated pixels, and at the low end to remove pixels with very low signal. The masking procedure aims to remove those pixels that are behind the beamstop. Doing this automatically is troublesome because there is some leakage of scattered signal either through the soft edges of a beamstop or as grazing incidence reflections off the hard edges. Any automated procedure will invariably remove too many pixels which can be costly at low spatial frequencies where much of the scattered power is located. Often, a hard mask, determined from one of the CCD exposures, is applied to all of the exposures. Finally, after normalization to exposure time and storage ring current, a weighted average can be calculated for each pixel. The result of this process for experimental data from a dry cell is shown in Figure 10. The final diffraction pattern is a 1200×1200 pixel subset of the full 1340×1300 pixel detector and represents a total x-ray exposure of just over 60 seconds, though the measurement require about 10 minutes to complete because of time spent moving motors and reading out the CCD. Of these 1.44 million measurements less than 400 are lost behind the beamstop. Unfortunately, this represents the 16 speckles with the most power, using the geometry at ALS beamline 9.0.1. The effect of this missing data is discussed in §5.2

Collection of a three-dimensional diffraction dataset requires rotation of the sample around at least one axis orthogonal to the x-ray beam. The rotation of the sample in real space is equivalent to the rotation of the Ewald sphere segment in reciprocal space. If we assume that the distance between Ewald sphere segments at the maximum scattering angle is equal to the sampling interval needed for critical sampling of the diffraction pattern then we arrive at an expression for the Crowther resolution:

$$\Delta\phi = \frac{\Delta q}{q_{max}} = \frac{\Delta x}{D} \quad (31)$$

where Δx is the real space pixel size and D is the object size. This level of angular sampling highly oversamples reciprocal space at low spatial frequencies and in practice is not needed since the iterative phase retrieval process is also capable of recovering missing intensities. An angular spacing of 1 degree has been adequate for 10 nm resolution reconstructions of 2 μm objects. The diffraction patterns recorded at each angle are recorded on a plane in reciprocal space though the spatial frequencies probed lie on the Ewald sphere surface. The location of this sphere in reciprocal space is described by:

$$q_z = \frac{1}{\lambda} - \sqrt{\frac{1}{\lambda^2} - q_x^2 - q_y^2} \quad (32)$$

Following Chapman *et al* this deviation of the sphere from the detector surface can be put in terms of the experimental geometry as [9]:

$$q_z = \frac{1}{\lambda} \left(1 - \frac{1}{z_D} \sqrt{z_D^2 - p^2(i^2 + j^2)} \right) \quad (33)$$

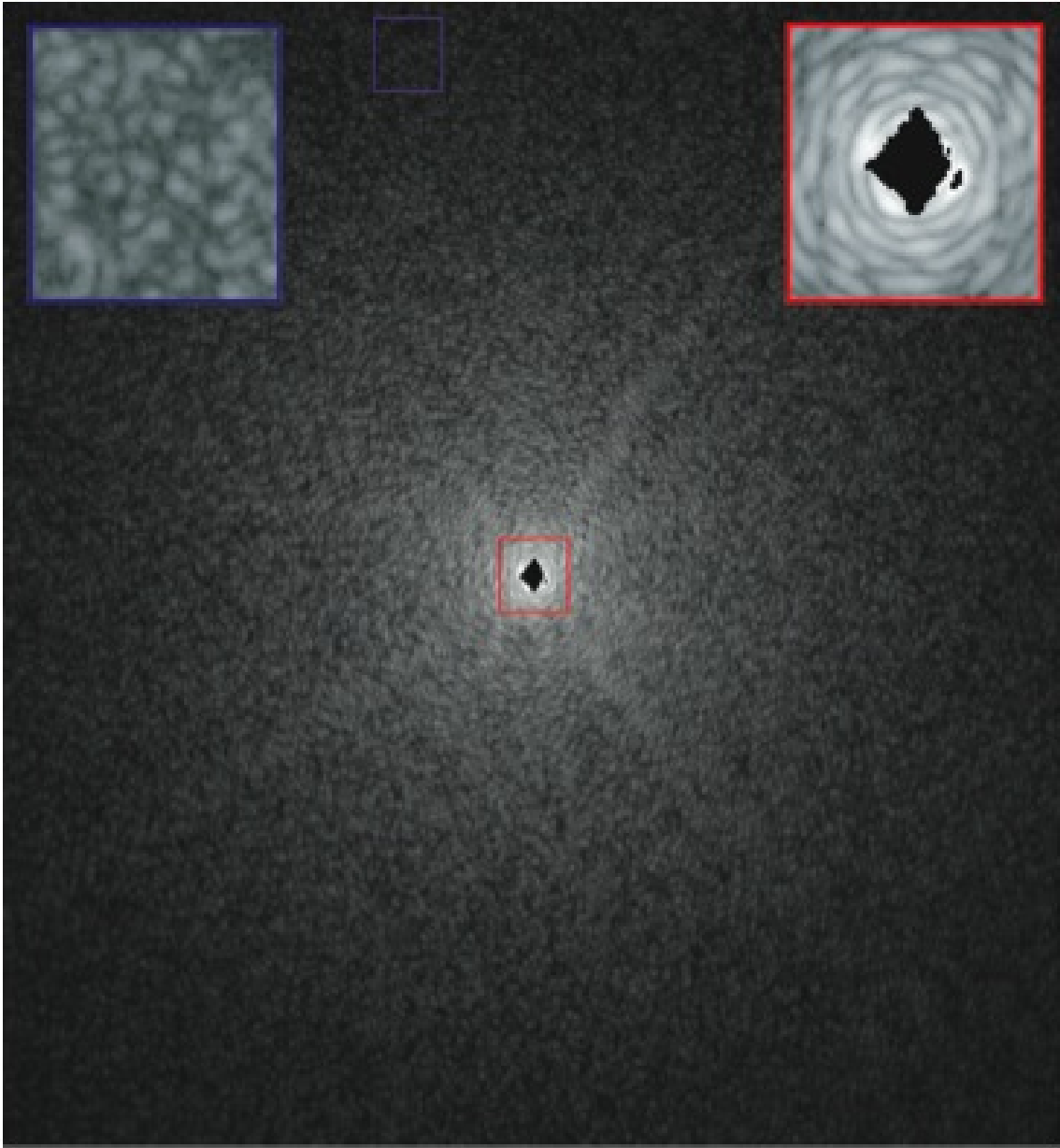


Figure 10: Fully assembled two dimensional coherent diffraction pattern of a freeze dried yeast cell using 750 eV x-rays. Individual CCD recordings are shown in Figure 9. Strong speckles can be seen to the edge of the detector (half period spatial frequency of 10 nm) with just 60 seconds of x-ray exposure (Reproduced from [13]).

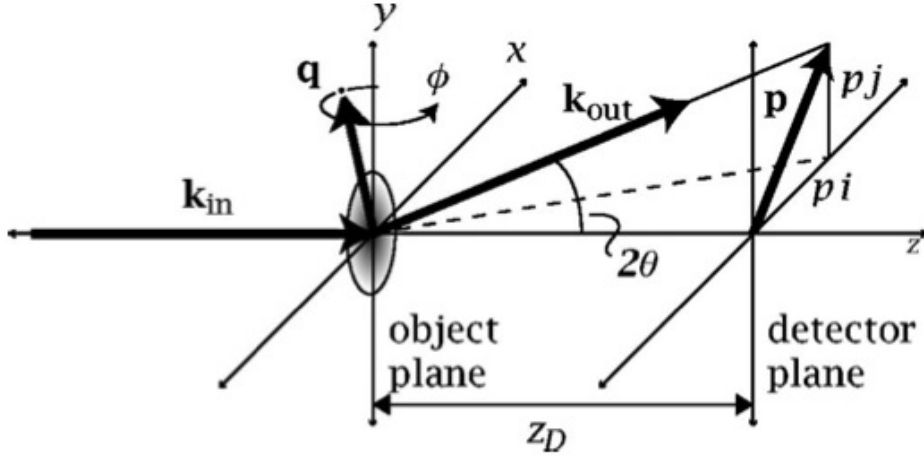


Figure 11: Geometry of coherent diffraction imaging measurements (Reproduced from [9])

where z_D is the distance between sample and detector and the vector $\mathbf{p} = p(\mathbf{i} + j\mathbf{j})$ is the location of a given pixel, with pixel size p , in the detector plane. Assembling the full three-dimensional diffraction dataset requires interpolation of the detector pixels into the voxels of a regular cartesian cube. The location of these voxels can be determined from the geometry shown in Figure 11 and in general is given by:

$$\mathbf{q}_{i,j} = \mathbf{k}_{out} - \mathbf{k}_{in} = \frac{1}{\lambda} \left(\frac{\mathbf{p}_{i,j} + z_D \hat{\mathbf{k}}}{\sqrt{|\mathbf{p}_{i,j}|^2 + z_D^2}} - \hat{\mathbf{k}} \right) \quad (34)$$

It is usually adequate to simply assign the value measured in the 2D detector plane to the nearest voxel in the 3D space. This is both because of the oversampling of the speckle pattern at low spatial frequencies and the undersampling at high frequencies. Typically, the two-dimensional diffraction pattern of a few micron object will have an oversampling ratio of at least ten, i.e. ten measurements per speckle. Thus sub-pixel errors in the location of that measurement in the 3D reciprocal space have a negligible effect. Furthermore, large distances between measurements at high spatial frequencies means that it is not feasible to spread them across multiple voxels since that would tend to reduce the measured intensity and also the reconstructed resolution.

4.2 Pre-Reconstruction Diagnostics

The simplicity of the coherent diffraction imaging experiment is both its greatest strength and weakness. The lack of any rapid real-space imaging capabilities makes sample screening very difficult and can result in the collection of lots of diffraction data that is either very difficult to reconstruct or of an uninteresting specimen. For this reason several techniques have been developed that can quickly provide information that allows the experimenter to judge either the quality of the specimen or the reconstructibility of the data. The most important quantity that can be calculated directly from the raw data is the samples autocorrelation function. This is a real space function but it can only provide very general information about the specimen structure. Perhaps the most important quality that can be judged from the autocorrelation is the sharpness of the specimen

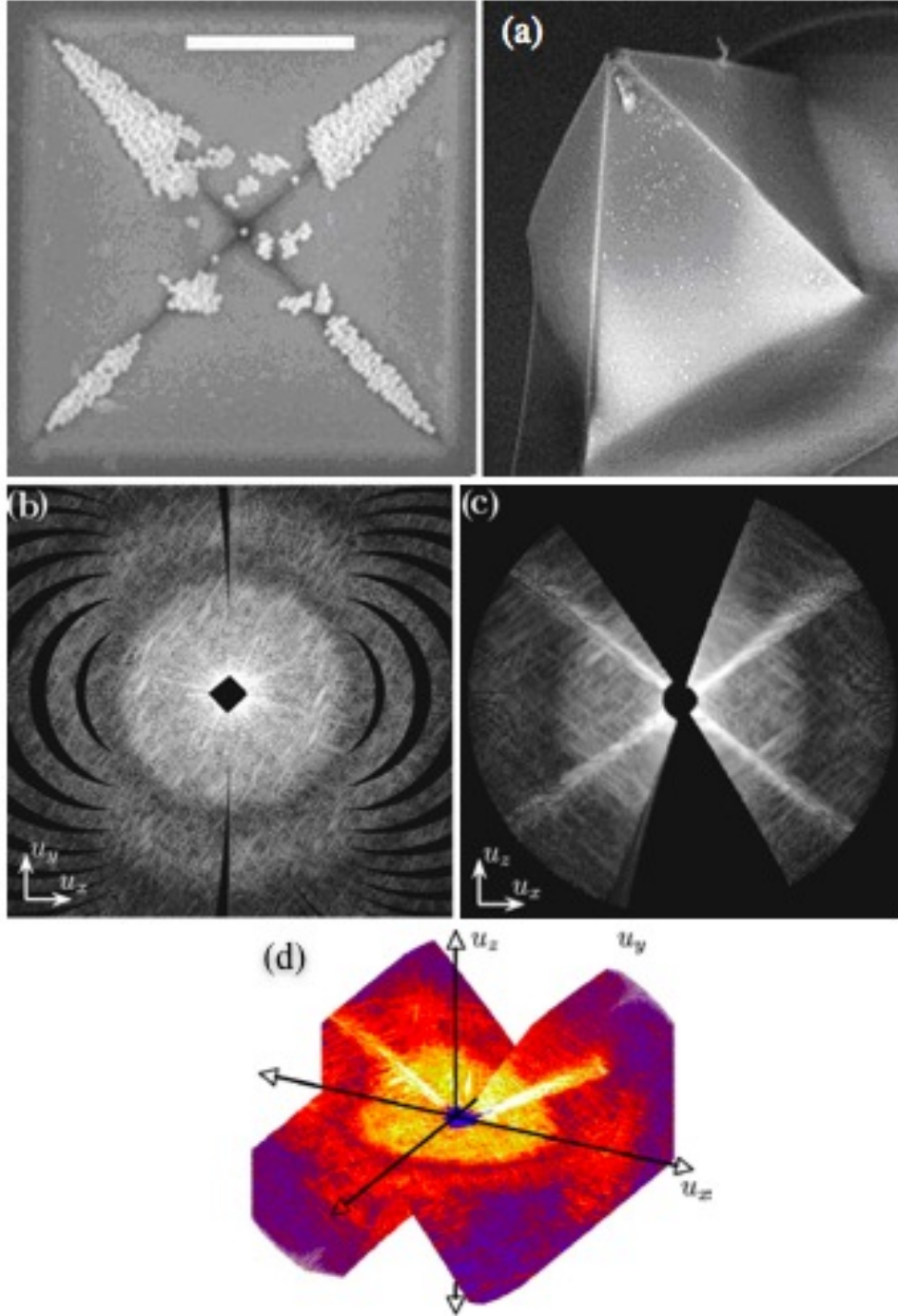


Figure 12: Three dimensional diffraction data. (a) three dimensional object consisting of a silicon-nitride pyramid that is decorated with 50 nm gold spheres. (b-c) Two dimensional slices through the origin of the full three dimensional diffraction pattern (principal planes). (d) 3D view of the full dataset. The principal planes show three sources of missing data: missing arcs due to coarse angular sampling, a missing wedge due to limited tilt angle, and the missing central region due to the beamstop (Reproduced from [9])

boundary. This is highly relevant to the reconstruction process since objects with very sharp boundaries are significantly easier to reconstruct. If an object is sharply bounded its autocorrelation will be sharply bounded. However, the CXDM setup can only measure a high pass filtered version of the autocorrelation which shows a sharp peak of intensity at its perimeter. Figure 13 shows the real part of the autocorrelation calculated from Figure 10. The sharp boundary as well as surrounding ghost images are apparent. These ghost images are the cross-correlation terms that result from interference between the specimen of interest and nearby dirt particles.

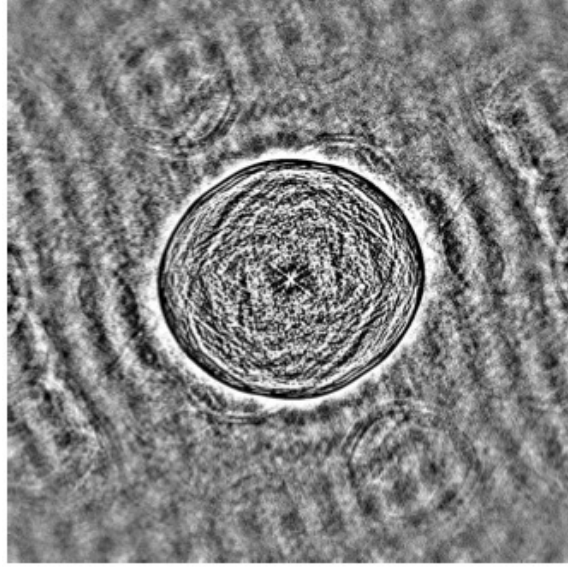


Figure 13: High pass filtered autocorrelation calculated from the diffraction pattern shown in Figure 10 (Reproduced from [64]).

The spectrogram technique can be used to inspect the data quality as a function of position across the 2D diffraction pattern. Just as the autocorrelation can be calculated from a high-pass filtered diffraction pattern it can also be calculated from a small sub-region of the full pattern. These versions of the autocorrelation should closely resemble each other but will be slightly different due to the different spatial frequencies represented. Figure 14 shows the spectrogram calculated from one of the diffraction patterns used in the gold pyramid reconstruction of Chapman *et al* [9]. Multiple regions of the spectrogram show a reduction in data quality arising from various sources. Regions at small scattering angles can be corrupted by scatter from the corner aperture and mounting membrane which results in intensity outside the support of the autocorrelation. A similar effect can be seen in regions containing the beamstop mounting arm where the signal-to-noise ratio is lower. These contaminated regions of the diffraction pattern can cause the shrinkwrap algorithm to fail by prohibiting support determination. To alleviate this problem Chapman *et al* applied a filter to the diffraction intensities which is equivalent to high pass filtering of the autocorrelation. This filter had the form:

$$f(\mathbf{q}) \propto q^4 e^{-q^2} \quad (35)$$

This method can work well for very high contrast specimens such as materials sciences samples but for biological samples, where the scattered intensity is weak and decreases rapidly with θ , the background scatter in the corrupted regions of the diffraction pattern needs to be carefully

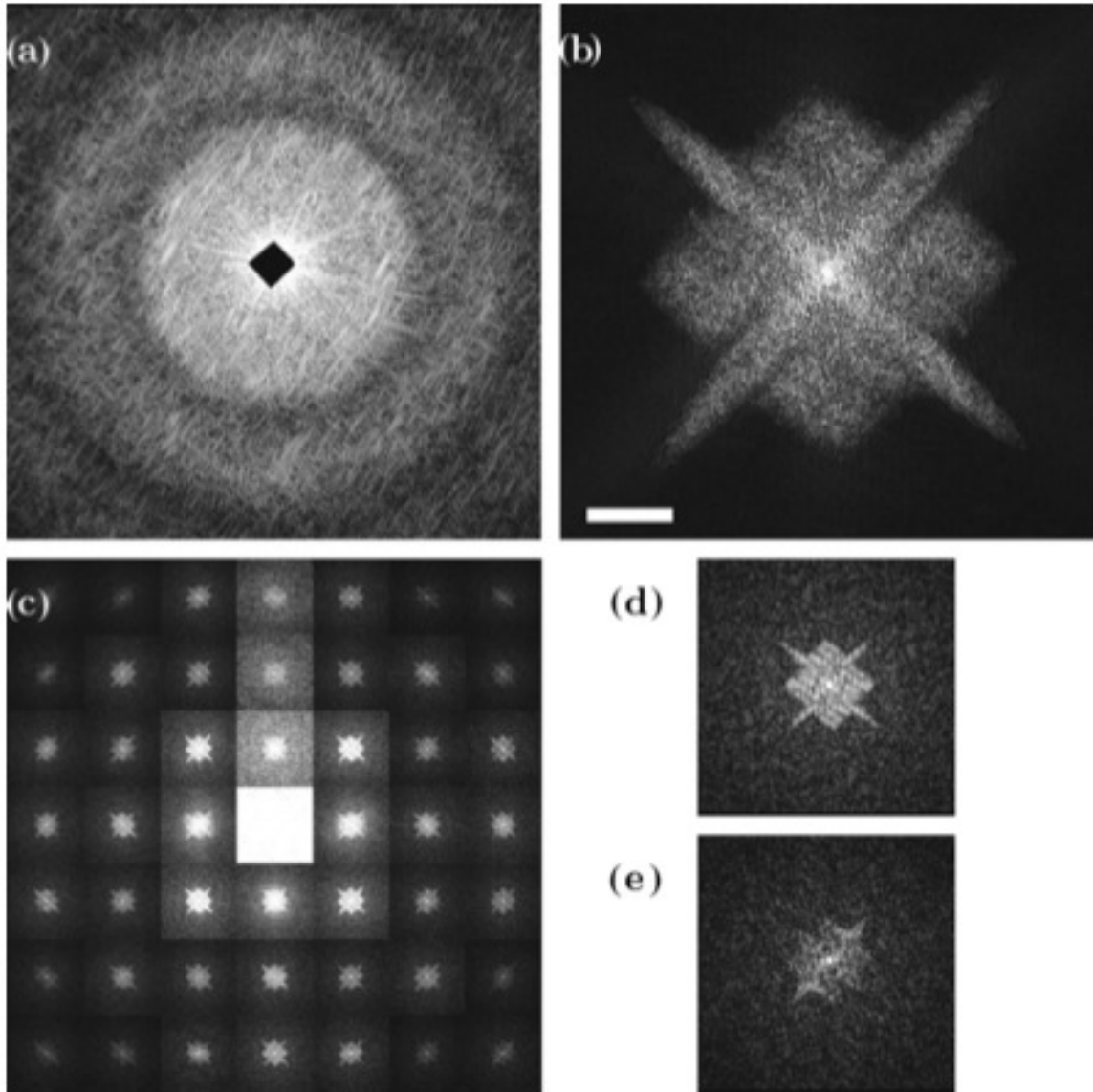


Figure 14: The spectrogram allows for a regional inspection of the quality of diffraction data. (a) two dimensional diffraction pattern assembled from a single angular view of the specimen, (b) autocorrelation calculated from (a), (c) spectrogram showing variation of the autocorrelations as a function of location within the field of view, (d-e) regional autocorrelations from the edge and corner of the detector respectively showing the loss of longitudinal coherence (Reproduced from [9]).

subtracted. A mathematical subtraction of the background is only feasible for scatter that is not coherent with the sample pattern. This holds true for scatter from the guard corner but not for scatter coming from dirt particles situated near the sample on the support membrane.

5 Image Reconstruction

Overwhelmingly, the greatest challenge to phasing diffraction data is the determination of the proper support. This is specially important for complex valued objects which require a tight support for full successful reconstruction [32]. The problem is greatly exacerbated by the missing data in the central region of the diffraction pattern. These low spatial frequency Fourier components contain most of the specimens power spectral density and provide much of the information contained in the large scale features such as the support shape. The unfortunate reality is that reconstruction attempts without a nearly exact support almost always fail while those with a tight support almost always succeed. Algorithms like Shrinkwrap have been developed to aid in support determination but they work best with samples that are very high contrast. This may usually hold with material sciences samples but it rarely holds with biological samples. Thus, support determination is a part of the iterative reconstruction process that requires a great deal of intervention on the part of the scientist. Often, early guesses at the support are made using estimates derived from the autocorrelation that have been edited on a pixel-by-pixel basis using an image editing program. Once a reasonably tight support is found this way, within on the order 10 pixels of the actual object boundary, shrinkwrap can be successful at optimizing its size.

A general process for image reconstruction is laid out in Figure 15. The sequence of images shows the effects of various steps of the process. The simulated data is calculated from a complex valued object, has an average photon noise per pixel of 25%, and is missing 0.2% of the pixels which contain 16% of the total power. These missing pixels are all located in the central portion of the pattern to simulate the effects of a beamstop (Figure 15(a)) though shrinkwrap is still able to determine the support because this is a reasonably high contrast object. The first reconstruction, top center, proceeds without support determination, i.e. without shrinkwrap, and without iterate averaging, a method of handling noisy diffraction data described below. The lack of a tight support completely prohibits successful reconstruction. The next two images have support determined by Shrinkwrap though the first proceeds without iterate averaging while the second proceeds with averaging. The next two reconstructions are started with the support previously determined by shrinkwrap and the first proceeds with iterate average while the second is an average of 25 random starts each of which proceeded with iterate averaging. The general trend of the sequence indicates first and foremost that tight support determination is absolutely essential and that averaging over random fluctuations that occur because of noise in the diffraction data can drastically improve the results. Though preliminary images can be obtained very quickly, reconstructing to the highest possible resolution requires averages over thousands of iterates and dozens of random starts. Table 2 shows the computational time for single three-dimensional reconstructions using highly optimized hardware and software [9]. The final images can take weeks to produce.

5.1 Image Averaging

Reconstructed images are corrupted by both high frequency and low frequency noise. The high frequency noise results from the low signal-to-noise ratio at the highest spatial frequencies measured

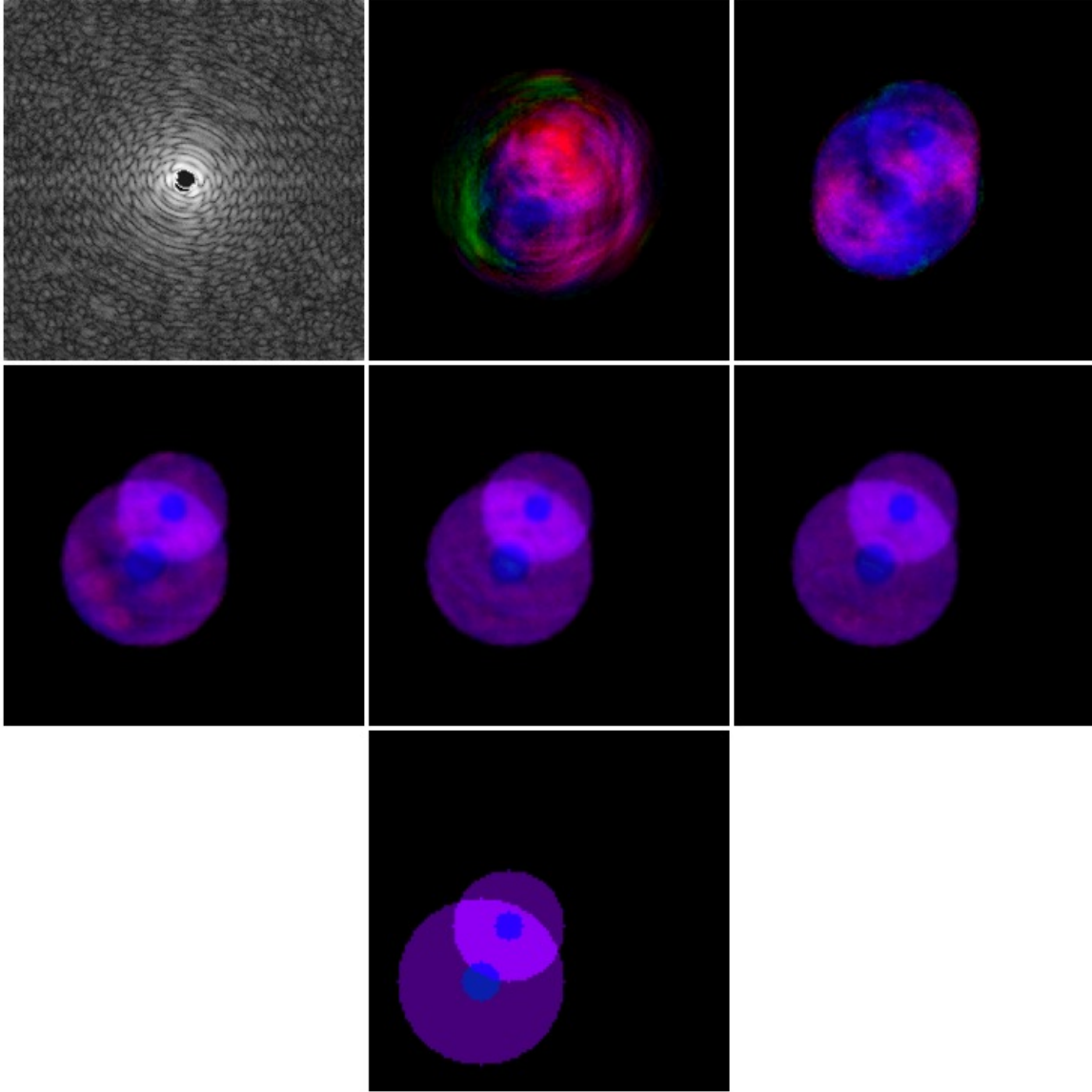


Figure 15: Reconstruction series. (a) Noisy diffraction pattern with an average of 25% noise per pixel and 16% missing power. (b-g) Reconstructions with: fixed loose support and without iterate averaging, shrinkwrap support determination but without iterate averaging, shrinkwrap support and iterate averaging, proper support and iterate averaging, proper support and random start averaging, actual solution. The final reconstruction is a blurred version of the original because of the presence of noise in the diffraction pattern. Images are color renderings of complex values such that hue is phase and saturation is magnitude.

Array Size	Single Precision	Double Precision	FFT	Reconstruction
256 ³	336 MB	592 MB	73 ms	10 min
512 ³	2.6 GB	4.5 GB	850 ms	1.5 h
1024 ³	21 GB	37 GB	7.9 s	14 h
2048 ³	168 GB	296 GB	?	?

Table 2: Memory requirements and calculation times for phase retrieval. Reconstructions were carried out on a 16 node cluster of G5 processors with two processors and 4 GBytes of RAM per node. [Reproduced from Chapman, 2006]

while the low frequency noise can result from systematic errors such as missing data, parasitic scatter, stitching errors from the data assembly process, and data missing behind the beamstop. High frequency noise is rapidly fluctuating and if not properly dealt with can relay a misleading degree of detail in the final image. Without quantitative analysis, the resolution of such images may appear higher than it actually is. The preferred method for removal of this noise, which leads to reproducible results, is to calculate the average over many iterates during the reconstruction from a single random start. Since the algorithm never settles down to a single solution, the average will be over all iterates in the vicinity of the solution and will be a lower resolution representation. The low frequency noise fluctuates much more slowly and can be smoothed out by averaging over many random starts. Since the constraints applied during reconstruction are blind to the global phase of the complex image it is not constrained and will tend to wander. Averaging over images with a different global phase will reduce the power in the image and lead to inconsistent results. The global phase of each image is therefore set prior to adding it to the average. The phase which minimizes the difference between the current image and the running average is calculated by,

$$\phi_0 = \arg(\langle \psi_{avg}^\dagger \psi_0 \rangle) \quad (36)$$

where the dagger indicates complex conjugation and the average is only calculated over the pixels inside the support. The image to be added to the average is then,

$$\psi_i = \psi_0 e^{-i\phi_0} \quad (37)$$

The averaged image will have reduced power in the Fourier components that have highly fluctuating phases. Thus the ratio of the Fourier magnitudes in the reconstructed and averaged image to the measured magnitudes gives a good indication of where phases are retrieved reliably and can be used to estimate the final resolution. The Fourier components that have highly fluctuating phases will have a reduced value for this ratio. This is analogous to the differential phase residual used in single-particle cryo-electron microscopy [41]. A transfer function for the phase retrieval process can be defined as a function of spatial frequency as,

$$PRTF(\mathbf{q}) = \frac{|\mathcal{F}[\langle \psi \rangle]|}{\sqrt{I_m(\mathbf{q})}} \quad (38)$$

where $\mathcal{F}[\langle \psi \rangle]$ is the Fourier transform of the final averaged image and I_m is the measured intensity pattern. An example of the phase retrieval transfer function is shown in Figure 16 which is calculated from the reconstruction of a freeze-dried yeast cell. The PRTF is compared to the modulation transfer functions of optics from an incoherent imaging system with Raleigh resolutions of 30 and

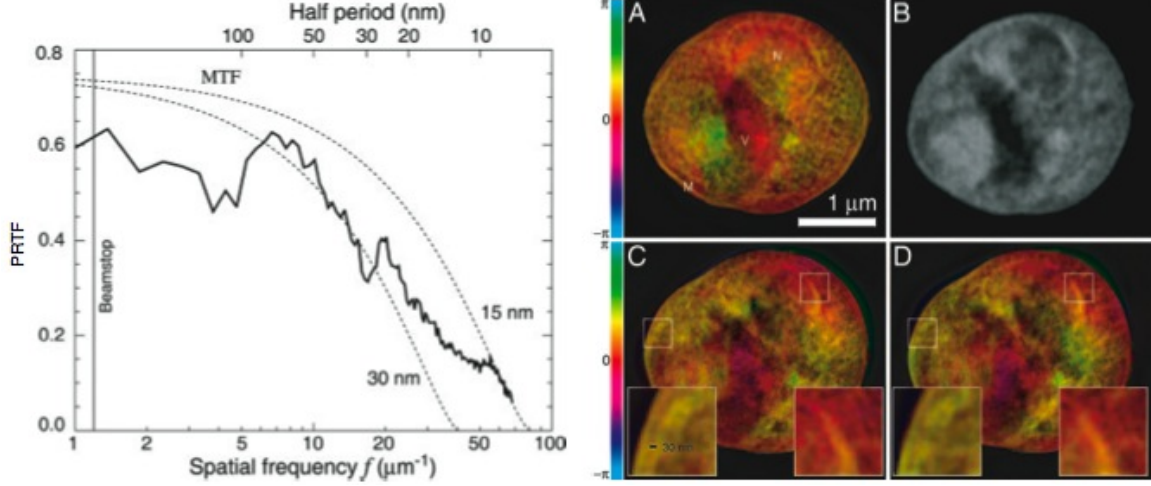


Figure 16: Left: PRTF of the reconstruction of a freeze-dried yeast cell. Right: (a) freeze-dried yeast cell reconstruction of Figure 10 and reconstructions from (c-d) multiple angular orientations of the cell. Features are reliably reproduced on the 30 nm size scale. This value of the resolution is corroborated by comparison of the PRTF to the modulation transfer function of an optic with a comparable Rayleigh resolution and comparison to a scanning transmission microscope image (d) using a 45 nm optic . (Reproduced from [61])

15 nm. These curves indicate an analogous resolution of the CXDM image of about 30 nm. This value is in good agreement with features that are reproduced in images calculated from independent datasets measured from two different angular orientations of the cell. Chapman *et al*'s somewhat more conservative choice of the resolution at which the PRTF drops to 0.5 would result in a resolution of about 40 nm. It is important to note that the actual resolution of the image is significantly lower than the pixel size even though there was strong diffraction signal all the way to the edge of the array used for reconstruction. This is due to the inconsistency of the constraints in the presence of random and systematic noise. Averaged images will have resolution below that allowed by the maximum scattering angle not only because of poorly retrieved phases but also due to a poorly determined support. If the support is larger than the actual object, even by a single pixel, the object will undergo random translations within that support once the algorithm has reached the steady state in the vicinity of the solution. Translations in object space are equivalent to a linear phase ramp in reciprocal space. If the perimeter of the object is more or less of continuous density then the support determined by shrinkwrap will have a constant distance from the true object. This distance r_0 gives a phase ramp in reciprocal space of $e^{i\mathbf{r}\cdot\mathbf{q}}$ with r_0 being the maximum slope. An average over all possible translations gives [64]

$$\langle \mathcal{F}[\psi] e^{-i\mathbf{r}\cdot\mathbf{q}} \rangle_r = \mathcal{F}[\psi] e^{-\frac{1}{2}r_0^2 q^2} \quad (39)$$

which is a gaussian low-pass filter. In addition to translation of the object within the support, a complex valued object can reconstruct out of focus in a loose support. Thibault *et al* argue that averaging over defocus planes, centered on the plane with smallest waist, and which are out of focus by a distance with standard deviation of z_0 also results in a gaussian low-pass filter of the form

$$\langle \mathcal{F}[\psi] \rangle_z = \mathcal{F}[\psi] e^{-\frac{1}{8}(z_0 q^2/k)^2} \quad (40)$$

In principle, a gaussian deconvolution of the final averaged image should be able to remove these filters though experimentally the effects could be alleviated by the placement of strong point like scatterers in the vicinity of the specimen.

5.2 Missing Data

Experimentally it is very difficult to measure diffraction data that is close to the unscattered x-ray beam. This missing area of the diffraction pattern, typically 20×20 pixels increases in angular size as the experiment moves towards recording higher resolution, i.e. decreases the distance between detector and specimen. In practice, this patch of missing data corresponds to 10-20 missing speckles. In itself, this precludes quantitative imaging because proper normalization of the center of the diffraction pattern is not possible. More importantly, serious artifacts can appear in the reconstructions if these regions of the data are not treated properly. The situation is a bit simpler for high contrast specimens which allow for the reconstruction of a high-pass filtered version of the object. The filter used by Chapman *et al*, equation (35), places a zero of intensity at the zero frequency pixel of the diffraction pattern which can tend to be the source of a phase vortex. Indeed, it was found that about 40% of the reconstructions, described below, from different random starts had a phase vortex centered on the center of the diffraction pattern. Comparison of all random starts prior to averaging allows for the removal of these vortex modes which in turn increases the PRTF since averaging of right-handed and left-handed vortices would reduce the reconstructed power. Higher order phase aberrations such as defocus, astigmatism, and coma can be found by fitting the recovered phase to the polynomial expansion [25]:

$$\exp[-ip(\mathbf{q})] = \exp[-i \sum_{i,j=0}^{i+j \leq n_p} p_{i,j} q_x^{-i} q_y^{-j}] \quad (41)$$

Reconstruction of a high-pass filtered version of the object may not work for lower contrast specimens. In those cases the full diffraction pattern as recorded needs to be used and the missing intensities at low spatial frequencies will be determined iteratively along with the missing phases. Unfortunately, in the absence of any sort of value constraint within the support in real space there is very little information available to constrain the missing intensities in Fourier space. Depending upon the shapes and sizes of the unconstrained regions in real and reciprocal there may be a set of mathematical functions which fit within the support and whose Fourier transformed counterparts also fit within the unconstrained region of reciprocal space. The power associated with these functions is unconstrained by the algorithm and can grow without bound. Following Thibault *et al* these unconstrained modes can be calculated as an expansion in quantum harmonic oscillator wavefunctions which are convenient because of their amplitudes that rapidly fall to zero outside of some boundary [64]. These wavefunctions are,

$$\psi_{n,m} = \frac{1}{\sqrt{\pi\sigma_x\sigma_y}} H_n(x/\sigma_x) H_m(y/\sigma_y) e^{-\frac{1}{2}(x^2/\sigma_x^2 + y^2/\sigma_y^2)} \quad (42)$$

where H_n is the nth Hermite polynomial and the gaussian widths, σ_x and σ_y depend upon the relative sizes of the unconstrained regions in real and reciprocal space. They are calculated as:

$$\sigma_x^2 = \sqrt{\frac{\frac{1}{N_s} \sum_r x^2 X_s(\mathbf{r})}{\frac{1}{N_f} \sum_r q_x^2 X_f(\mathbf{q})}} \quad (43)$$

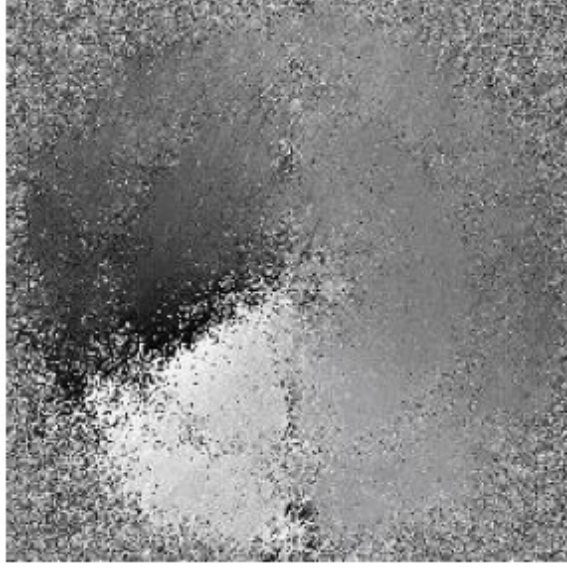


Figure 17: The difference of recovered phases from two reconstructions of the pyramid data indicate the presence of a phase vortex mode in one of the reconstructions. Removal of these modes from the average increases the recovered resolution (Reproduced from [25]).

and

$$\sigma_y^2 = \sqrt{\frac{\frac{1}{N_s} \sum_r y^2 X_s(\mathbf{r})}{\frac{1}{N_f} \sum_r q_y^2 X_f(\mathbf{q})}} \quad (44)$$

where N_s and N_f are the number of unconstrained pixels in real space and reciprocal space respectively and X_s and X_f are two-dimensional binary masks representing the locations of those pixels. Ultimately, we are interested in finding the amplitudes of the modes with the least constrained power. In this case, an eigensystem can be written as

$$\lambda_{n,m} \psi_{n,m} = W \psi_{n,m} \quad (45)$$

where W is the constrained power operator whose matrix elements,

$$W_{i,j} = \sum_{\mathbf{r}} X_s \psi_{n_i, m_i}^* \psi_{n_j, m_j} + \sum_{\mathbf{q}} X_f \mathcal{F}[\psi_{n_i, m_i}]^* \mathcal{F}[\psi_{n_j, m_j}] \quad (46)$$

give the constrained power per mode after diagonalization. An upper bound on the number of missing modes to be calculated can be estimated from the number of unconstrained pixels as,

$$M = \frac{N_s N_f}{N^2} \quad (47)$$

though in practice the amplitudes of only the first few modes need to be controlled to produce visually plausible reconstructions. Figure 18 shows the four least constrained modes of the reconstruction in Figure 16(a). The zeroth mode has a constrained power of 0.00017%. Though the precise amplitudes of these modes cannot be determined by the diffraction data it is possible to set

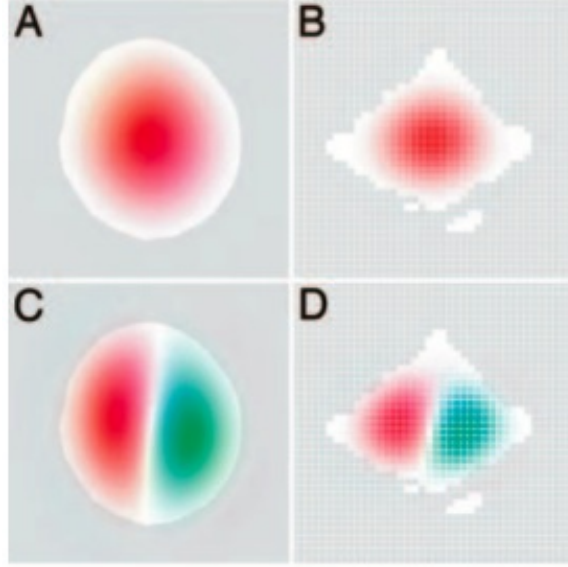


Figure 18: Two least constrained eigenmodes of constrained power operator calculated for the yeast reconstruction shown in Figure 16(a). Left images show the modes in real space and the right show reciprocal space (Reproduced from [64]).

their values in such a way that the information that is constrained by the diffraction data can be more easily interpreted. Since we are ultimately interested in the rapidly changing features of small amplitude it seems reasonable to require that the mode amplitudes be set to values that flatten the image. Thibault *et al* suggest an *ad hoc* procedure that involves minimizing the variance of the reconstructed values within the support. Figure 18(c) shows the effect of this minimization. All three images are equally valid in that they all satisfy the Fourier modulus and support constraints but the first two images are difficult to interpret because of extreme amplitudes of the unconstrained modes. The image with variance minimized clearly shows the high spatial frequency information that we are interested in.

5.3 Resolution analysis

The ultimate evaluation of resolution requires knowledge about the object that is being imaged. Thus resolution is typically evaluated using a known object rather than an unknown object. But for phase contrast imaging, resolution depends on the sample in addition to the instrument. But if the resolution depends on the object, we need to rely on other proofs, which are subject to continuing debates.

Indirect imaging techniques that rely on numerical optimization methods can only rely on the assumption that if the solution is unique, it satisfies the constraints, fits the data, and therefore it must be true. Only an exhaustive search can prove uniqueness, but confidence that the solution is unique is given by running the reconstruction algorithm with different random starts. If the algorithms converge reliably to the solution, we assume that the solution is unique. We can screen for bad algorithm runs and select only the runs that successfully fit the data within the noise level. Instabilities in the solution are quantified by the statistical properties of the reconstructed phases

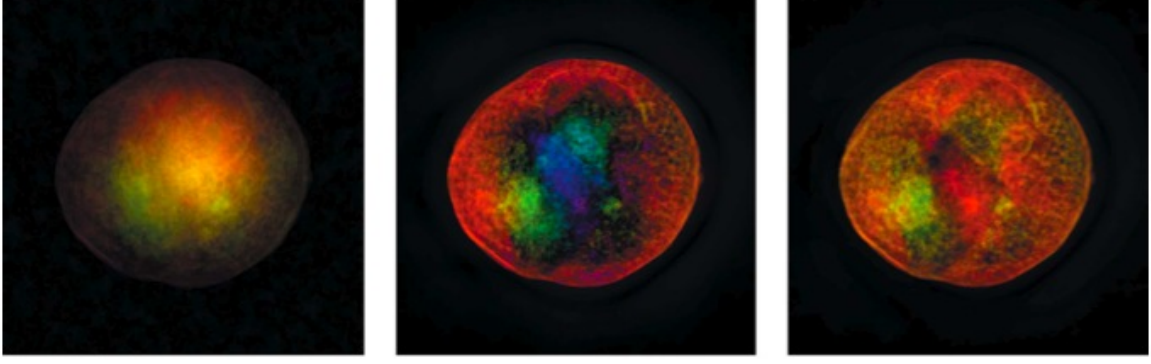


Figure 19: Reconstruction of Figure 10 with different amplitudes for the four least constrained modes. (a) amplitudes left to vary freely, (b) amplitudes zeroed, and (c) amplitudes set to minimize variance of the pixel values within the support.

at various \mathbf{q} . We re-write the phase retrieval transfer function described above as:

$$PRTF(\mathbf{q}) = \frac{|\langle \Psi \rangle|}{\sqrt{I_m(\mathbf{q})}} \quad (48)$$

where $\langle \Psi \rangle$ is the Fourier transform of the final averaged image.

A simple and intuitive relation between transfer function and rms errors, allows us to quantify not only errors resulting from noisy information, but some systematic errors resulting from incorrect information as well. The transfer function is related to the normalized standard deviation σ_{PR} of the recovered complex Fourier amplitude pattern Ψ [25]:

$$\sigma_{PR}(\mathbf{q})^2 = \frac{\langle |\Psi(\mathbf{q}) - \langle \Psi(\mathbf{q}) \rangle|^2 \rangle}{|\langle \Psi(\mathbf{q}) \rangle|^2} \quad (49)$$

by the following equation:

$$TF(\mathbf{q}) = \frac{1}{\sqrt{1 + \sigma^2}} = \frac{|\langle \Psi(\mathbf{q}) \rangle|}{\sqrt{\langle |\Psi(\mathbf{q})|^2 \rangle}}. \quad (50)$$

If we assume that $|\Psi| = \sqrt{I_m}$, the denominator reverts to $\sqrt{I_m}$ used in the original definition of the PRTF (eq.48), but the transfer function is generalized in regions where this information is missing.

Once we have established that the solution is unique or close to it, we need to verify that it is correct. Having too few constraints can result in instabilities in the reconstruction, but the constraints may be wrong, for example if the support was smaller than the actual object. If the support is too tight, for example by only a single pixel, the reconstructed image will be unique but wrong. To quantify the fit to the data, we use the normalized standard deviation between measured intensity values and recovered ones, after enforcing the support constraint:

$$\sigma_{RF}^2(\mathbf{q}) = \frac{||\Psi(\mathbf{q})| - \sqrt{I(\mathbf{q})}|^2}{|\sqrt{I(\mathbf{q})}|^2} \quad (51)$$

and define a transfer function as:

$$RTF(\mathbf{q}) = \frac{1}{\sqrt{1 + \sigma_{RF}^2}} \quad (52)$$

In addition, the signal to noise properties of the data contribute to the final estimate of resolution using similar relations. If the product of these transfer functions is close to 1, we can be fairly confident that the reconstructed structure is unique and correct, in the sense that it satisfies both the measured data and the constraints.

5.4 Three-dimensional objects

Two dimensional objects, $O(x, y)$ may be represented by a three-dimensional Fourier transform whose third axis is constant in q_z , since in the third real space dimension, the object is actually a delta function. However, the frequencies represented in a two dimensional measurement of this reciprocal space still lie on a segment of the Ewald sphere. The distance between the sphere and the plane $q_z = 0$ is $q_z = \theta^2/(2\lambda)$ where this is a maximum when the scattering angle is equal to the numerical aperture of the microscope which is typically around 0.1. For two dimensional objects, the diffraction pattern is independent of this distance up to terms quadratic in q_x and q_y . Three dimensional objects, however, have variation of the Fourier amplitudes along the q_z direction and measurement of these amplitudes on the Ewald sphere instead of a principal plane results in defocus effects in the reconstructed image. These effects are negligible if the object is thin enough that even at the highest spatial frequencies the Ewald sphere still cuts through a speckle which is centered on $q_z = 0$. It is reasonable then that the thickness requirement for an object to be fully in focus is that the departure be no more than one quarter of the speckle width [9],

$$\frac{\theta_{max}^2}{2\lambda} < \frac{1}{4D} \Rightarrow D < \frac{\lambda}{2\theta_{max}^2}$$

For a NA of 0.1 and wavelength of 1.65 nm (750 eV) this gives a thickness of 83 nm. Clearly this indicates that most samples of any practical interest will have significant defocus effects when imaged in only two dimensions. A further consequence is that even real valued objects will reconstruct as complex which means that the powerful positivity constraint cannot be applied. Large variations in the complex amplitudes will arise because of the propagation of the out of focus regions of the image. The reconstruction algorithm will tend to reconstruct the support in the focal plane which maximizes the overall contrast of the image. Other regions of the image can then be brought into focus by Fresnel propagation. This is illustrated in Figure 20 which shows a reconstruction of one of the views used to assemble the full three-dimensional pattern in figure 12. Figure 12(a) shows the image as provided by the algorithm while (b-c) show the same image numerically propagated forward and backward. Lineouts from two points as a function of propagation distance show the ability to focus on different depths of the image. Since all three images have identical diffraction patterns, i.e. power as a function of spatial frequency, this sequence is not equivalent to optical sectioning which would reduce the power present in the image from the out of focus regions.

6 Applications

Since the initial demonstration by Miao *et al* in 1999, the field of CXDM has grown to include hundreds of scientists doing research at a half dozen synchrotron light sources around the world. The resolutions and specimen sizes available to CXDM give it the potential to be a powerful tool in cell biology, many areas of materials sciences, and as we will see, ultrafast science. Indeed, in the

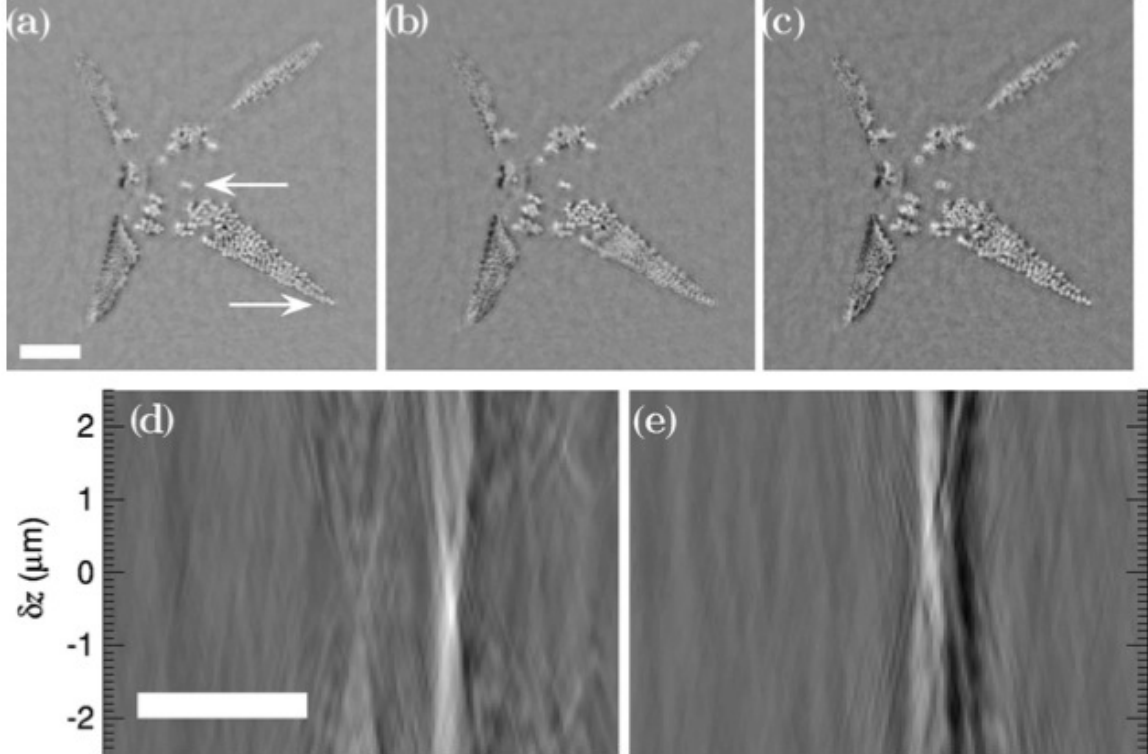


Figure 20: Two-dimensional views of three-dimensional objects show defocus effects. (a) actual reconstruction from the data in Figure 14(a), (b-c) reconstruction in (a) propagated $-0.5 \mu\text{m}$ and $+0.7 \mu\text{m}$ respectively. (d-e) lineouts from indicated in (a) for different propagation distances. The difference in focal plane is apparent. (Reproduced from [9])

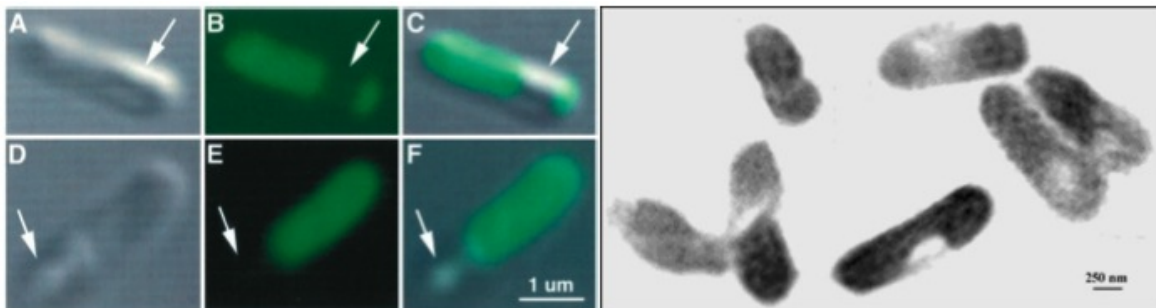


Figure 21: Left: visible light microscope images of *e. coli*. (a,d) transmission images, (b,e) fluorescence images, (c,f) overlay of transmission and fluorescence images. Right: CXDM image using 2 Å x-rays. The dark regions are dense with protein bound with $KMnO_4$ and a yellow fluorescent protein (Reproduced from [51]).

past decade CXDM has been used to image biological cells, ultra-low density foams, metallic nanocrystals, and quantum dots among other things. All of these demonstrations provided resolutions and sample characteristics that no other imaging technique is capable of probing.

6.1 Cell Biology

Budding yeast, *Saccharomyces cerevisiae*, and *Escherichia coli* bacteria are model systems for molecular, biochemical, and genetic studies. The yeast proteome is comprised of thousands of proteins that combine into hundreds of multi-protein complexes which can participate in tens of thousands of unique interactions. The ability to localize these complexes within the natural cellular environment is crucial to understanding the function and linking of cellular pathways. Three-dimensional x-ray imaging is likely to be a valuable complement to cryo-electron and visible light microscopy for these studies because of the ability to image whole frozen cells. Transmission x-ray microscopy with diffractive optics has the advantage of higher throughput but CXDM can image at high resolution with extended depth of focus and with high efficiency. This may prove to be crucial for the visualization of individual macro-molecules within the cell.

By the preparation of this manuscript there have been two demonstrations of CXDM of biological systems: one using hard x-rays with a wavelength of 2 Å and the other using soft x-rays with a wavelength of 16.5 Å. The first demonstration, due to Miao, is shown in Figure 21 [51]. In this case, *escherichia coli* cells were labelled with a recombinant protein containing six histidines and a yellow fluorescent protein. The cells were then incubated in a $KMnO_4$ solution which binds to the histidine sequences and greatly increases the hard x-ray scattering strength providing adequate contrast. The reconstructed image shows large scale features that are in good agreement with the visible light images and fine features that are not resolved in the visible images. The diffraction pattern used for the reconstruction, however, was missing 70×70 pixels in the center due to saturation of the CCD. These pixels, 2% of the total, were filled in with intensities calculated from a transmission x-ray microscope image and represent about 60% of the total power in the image.

The second demonstration, due to Shapiro *et al*, provides a stereo image of a freeze dried yeast cell at 30 nm resolution (Figure 22) [61]. In this case, the cell is unlabeled and freeze-dried by rapid freezing followed by slow warming under vacuum. The rapid freezing prevents destruction of cell features from the formation of ice crystals while the slow warming under vacuum allows for the

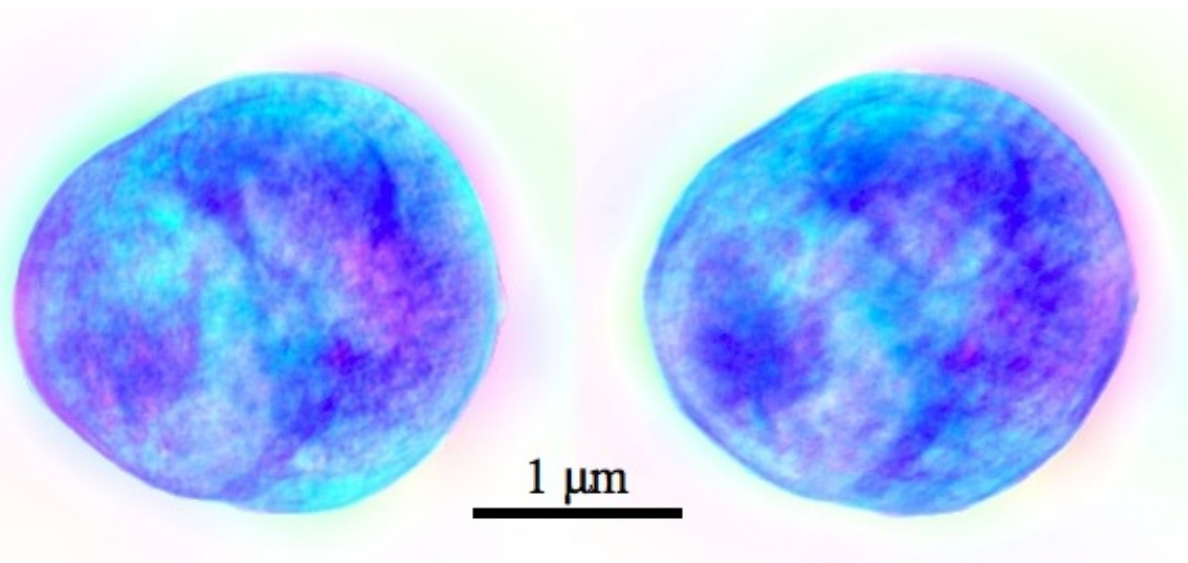


Figure 22: Complex valued, stereoscopic image of a freeze-dried yeast cell obtained by phasing the diffraction data similar to that shown in Figure 10. The angular separation of the images is 5 degrees. Phase information is represented as hue and magnitude is saturation using the HSV color scheme. The resolution of 30 nm is estimated from the phase retrieval transfer function shown in Figure 16.

removal of ice by sublimation, leaving much of the large scale cell structure intact. The resolution of this particular reconstruction is determined using the PRTF method and is somewhat lower than the maximum resolution achievable with the detector numerical aperture. This is presumably due to an insufficient signal-to-noise ratio (SNR) at the detector edge. Chapman *et al* have shown that the iterative phase retrieval algorithms will adequately phase diffraction data out to a spatial frequency with a SNR of approximately 1.

Stereoscopic viewing (achieved by focusing ones eyes at a point in front of the image) reveals significant three-dimensionality in the image. This provides the possibility of using stereoscopy as a low-dose form of three-dimensional imaging [15]. The relative orientations of major cellular organelles can be determined and, if the resolution is increased to 5-10 nm, large macro-molecular protein complexes may be counted or even identified. Identification of protein complexes, however, will likely require the information content available only in full three-dimensional images. To this end, several research groups are developing coherent diffraction microscopes capable of handling frozen-hydrated samples. Maintaining a hydrated cell in a pristine cryogenic environment is technologically challenging but ultimately will provide the protection against radiation damage needed for the highest resolution imaging. Howell's *et al* have assembled data from the literature that indicate a rough relationship between the dose required to destroy frozen-hydrated organic features and the size of those features [23]. Several independent calculations of the dose required for imaging at a given resolution indicate that the radiation damage limited resolution for CXDM will be in the neighborhood of 5-10nm [16, 23, 54]

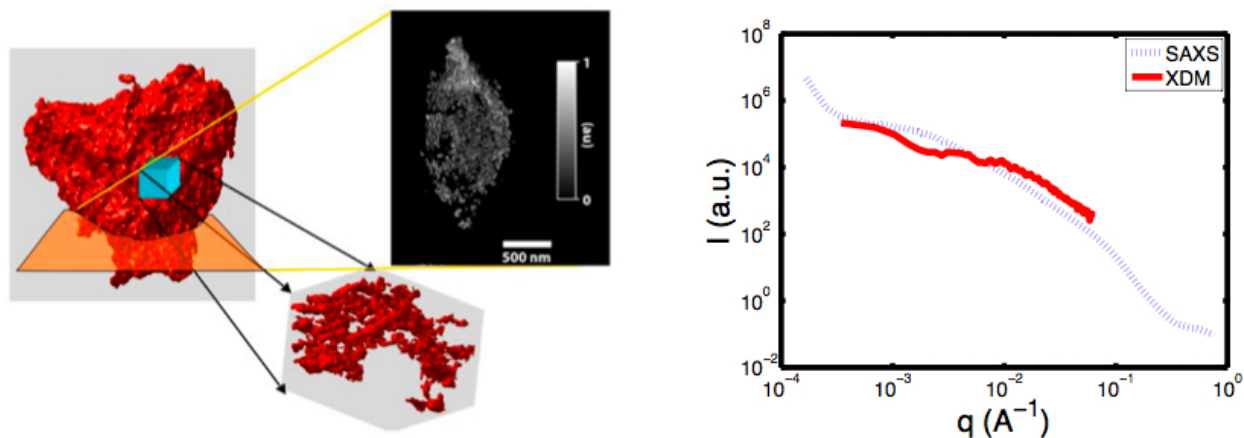


Figure 23: Reconstruction of a tantalum-oxide nanofoam. Left: surface rendering of the full reconstruction, surface rendering of a 500 nm sub-volume, and a slice through the interior. Right: comparison of the power spectrum obtained from the coherent diffraction image and that obtained from small-angle x-ray scattering (Reproduced from [19]).

6.2 Materials Science

Diffraction microscopy promises even higher resolution images of materials which are not sensitive to ionizing radiation exposure. Nano-porous materials are an important class of materials with applications ranging from the diffusion of oil through rock to the efficient storage of hydrogen as fuel. In general, it is desirable to have materials which are light weight, strong, and have a very high surface area. With pore sizes of typically 1-100 nm and mechanical properties that depend on the bulk structure, high resolution diffraction microscopy is ideally suited to study these materials.

An important demonstration of such a study is provided by Barty *et al* who studies a tantalum-oxide nanofoam (Figure 23) [19]. The Ta_2O_5 foam is an ultra-low density, high- Z material that is used in double-shell laser ignition fusion targets. The three-dimensional diffraction pattern was recorded using 750 eV x-rays and reconstructed using the RAAR algorithm with iterative support determination by *Shrinkwrap*. The result is a material density map at 15 nm resolution which displays a "blob and beam" structure that can be explained by the diffusion-limited cluster aggregation model. This particular structure is weak because of bending of the "blob" type nodes and computer simulated thinning of such nodes shows marked increase in material strength.

A related technique developed by Robinson *et al* investigates strain fields in metallic nano-crystals [39,53]. When using sufficiently hard x-rays, if a small crystal is fully coherently illuminated then there will be diffuse x-ray scatter around the Bragg peaks. The form of this diffraction pattern is due to the overall morphology of the crystal and any break from centro-symmetry is due to phase shifts within the crystal arising from mechanical strain fields. Phasing the oversampled Bragg peaks will result in a complex density that represents both the crystals electron density (as magnitude) and any strain fields present (as phase). This technique has been demonstrated by Pfeiffer *et al* with a small lead crystal at about 40 nm resolution and promises to provide valuable information about crystal defects and grain interactions (Figure 24). Similarly, it has been suggested that the same technique could be applied to frozen hydrated protein nano-crystals at a resolution adequate to see every unit cell within the crystal. Such studies, often carried about by atomic-force microscopy, may

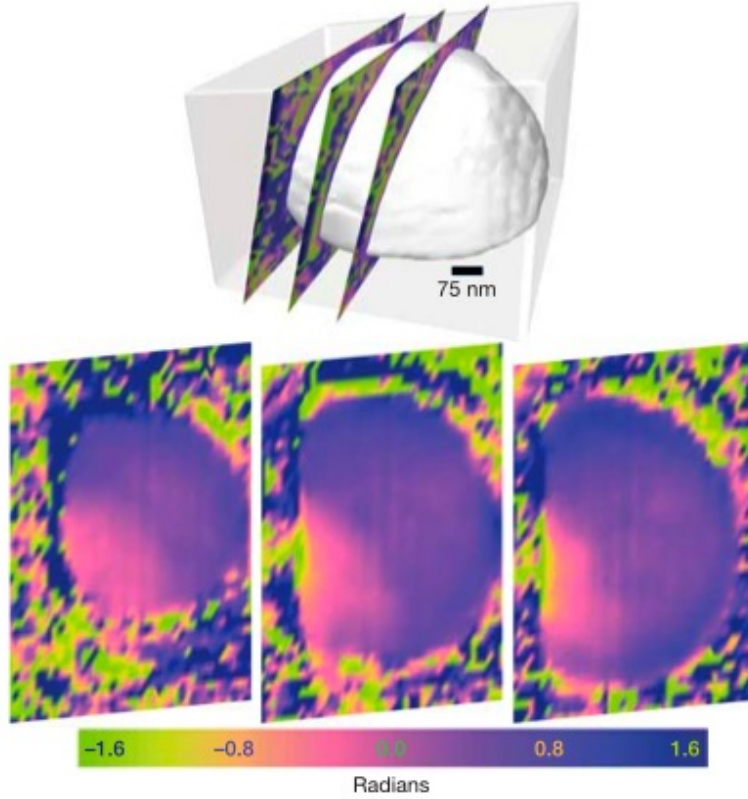


Figure 24: Reconstruction of the strain field in a lead nano-crystal. Top: surface rendering of the reconstructed electron density. Bottom: slices through the three-dimensional phase map. The phase of the complex valued reconstruction is related to the crystalline strain field projected in the direction of the Bragg peak measurement (Reproduced from [53]).

help to explain why many proteins fail to form crystals larger than a few hundred nanometers [60].

The chemical specificity of x-rays is widely exploited in the field of spectromicroscopy which uses a scanning microscope to acquire x-ray spectra at points on a regular grid around the sample of interest. This "stack" of images provides a three-dimensional dataset (two spatial dimensions and one energy dimension) that allows for the study of the spatial distribution of different chemical species. The high resolutions achievable with a coherent x-ray diffraction microscope require lengthy exposures times and indicate that such a stack of images, though possible in principle, is probably not practical. However, it is reasonable to acquire two such images on opposing sides of an elemental absorption edge in order to map out the spatial distribution of the particular element. This technique has been demonstrated by Song *et al* who image the distribution of Bi in a doped silicon crystal [63]. Diffraction patterns are recorded immediately above and below the Bi M_5 edge and then phased independently. The difference of the two reconstructions indicates the change of the complex electron density across the edge which should roughly map out the locations of high bismuth density (Figure 25). This technique is non-destructive, allows for the imaging of buried structures, and given suitable brightness and photon energy could in principle be extended to atomic resolution.

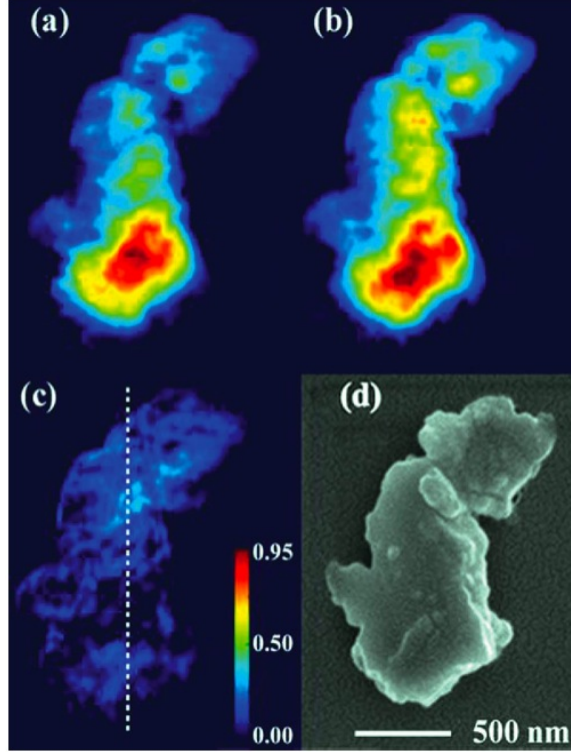


Figure 25: Resonant diffraction microscopy of a Bi doped silicon crystal. Images (a) and (b) are diffraction images recorded below and above the Bi M_5 edge respectively. Image (c) is the difference which roughly indicates the projected distribution of Bi atoms. Image (d) is an SEM image of the same particle (Reproduced from [63]).

6.3 Hybrid Methods

It is now generally recognized that David Sayre's dream of realizing 3D imaging by simply rotating an object in a homogeneous field of coherent light has several experimental advantages. As soon as one starts shaping the beam with optical elements, one pays a premium both from the point of view of being able to get different views (rotations will move the object laterally with respect to the beam) and also the experiment becomes affected by vibrations. By removing the need for any optical element, diffractive imaging remains the best candidate to achieve high-resolution ultrafast single shot flash imaging beyond the radiation damage limit.

Despite numerous successful experimental results, however, the solution to the phase problem remains a challenging task, and novel schemes have been proposed to build on the strength of diffractive imaging, while aiding the numerical reconstruction through beam shaping. A review of these schemes is beyond the scope of this chapter though we point out some recent development in this direction that is by no means exhaustive.

One scheme is Fourier transform holography, discussed elsewhere in this book. By adding a reference point source next to the specimen, one obtains a holographic image by direct Fourier transform of the diffraction pattern. This was demonstrated experimentally for soft x-rays by Eisebitt *et al.* and is discussed elsewhere [17]. A second scheme is point-projection holography.

A point source is produced upstream of the specimen, so that it is illuminated by a diverging wave. Thus, although the measurement takes place in the far field, the diffracted wave is related to the object via the Fresnel diffraction formalism so that one obtains a magnified version of an inline hologram [21,34]. The addition of phase retrieval schemes allows extension of the resolution beyond the source size. The third scheme, known as ptychography, is a hybrid method between scanning transmission x-ray microscopy and diffractive imaging. The diffraction patterns recorded at multiple positions provide such an abundance of information that not only is the reconstruction process much faster and more robust, but it also allows the reconstruction of the incident wavefront [43]. The concept of ptychography was originated by the late Walter Hoppe around 1969 [65,66] but two key developments have made the case for this technique extremely compelling. One is the advent of fast detectors, and the other was the adaptation of the algorithms developed for single particle diffraction phasing [24]. As fast detectors become more widely available, ptychography could potentially become the method of choice in all scanning transmission beamlines around the world [38].

6.4 Ultrafast Science

The development of fourth generation synchrotron x-ray sources (free-electron lasers or FELs), with their orders of magnitude increase in peak brightness and ultra-short pulses, promises to allow near-atomic resolution imaging of small radiation sensitive materials. In conventional microscopes, including CXDM, the resolution is ultimately limited by structural changes in the sample due to the energy deposited by the probing radiation. Molecular dynamics simulations indicate that within about 10 fs after x-ray photo-absorption, the photo-electrons, Auger electrons and shake electrons are emitted while thermal diffusion and free-radical effects can take up to milliseconds [26,56,67]. If an x-ray pulse is very short and bright then high resolution structural information can be captured before these processes are manifest. This is particularly advantageous for small particles for which there exist many identical copies such as proteins and protein complexes. Though a single x-ray pulse will damage one molecule there exist many more that can contribute to the diffraction pattern. This allows for the collection of three dimensional data, by recording diffraction from identical proteins in different orientations, and it allows for increased signal at large scattering angles by averaging over many proteins in similar orientations. The challenging requirement then becomes to have all of the proteins in the same conformational state, and to be able to classify protein orientation from the noisy pattern that a single x-ray pulse will produce. Algorithms have been developed that classify diffraction patterns by exploiting the "common lines", the region of reciprocal space shared in common between two arbitrarily oriented planar or spherical sections, though simulations indicate that an unpractical level of signal is required for success [28]. Other algorithms that utilize all of the points measured in a single diffraction pattern, and therefore may reduce the signal requirement, are under development.

The first steps towards the "diffract and destroy" method of protein structure determination have been made using the low energy FEL's currently available [6,20,37]. These light sources provide the brightness required for ultra-fast imaging but have wavelengths that only allow imaging at a few tens of nanometers resolution. Chapman *et al* have used a fabricated test object to demonstrate that, though the sample is destroyed by a single FEL pulse, the diffraction pattern it produces can be used to reconstruct a high resolution image of the destroyed object. In this case, the VUV-FEL FLASH delivered a single 25 fs pulse of 32 nm wavelength photons to the sample. With 10^{12} photons per pulse the first pulse instantly vaporizes the sample, a silicon nitride window with holes

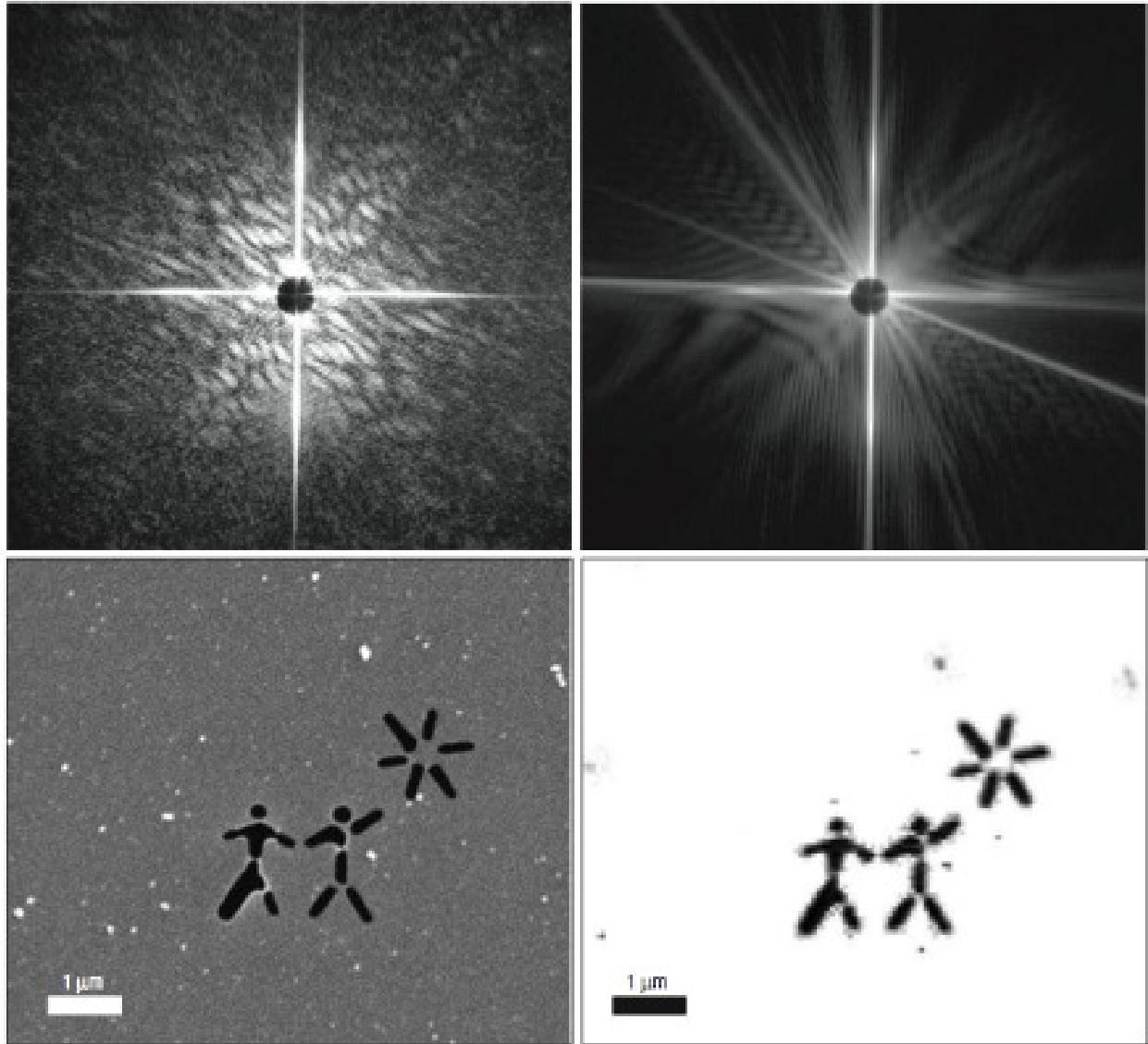


Figure 26: Ultra-fast diffraction imaging with an FEL. Top left: diffraction pattern from the first 25 femtosecond pulse shows strong speckles from interference with the object. Top right: diffraction pattern from the second pulse shows that the object was destroyed by the first pulse. Bottom left: SEM image of the test object made by removing material from a silicon nitride window using a focused ion beam. Bottom right: diffraction limited image reconstructed from the first pulse (Reproduced from [37]).

removed by a focused ion beam, and the second pulse shows the remains (Figure 26). The single pulse carried enough photons to allow adequate signal for a diffraction limited resolution of 62 nm. Subsequent experiments at FLASH have utilized a pump-probe geometry with a variable time delay. These experiments use a femtosecond laser pulse to vaporize the sample and then the FEL pulse to provide images of the material at various times during the explosion. This technique could be used to study mesoscale dynamics with a temporal resolution of a few tens of femtoseconds. The march towards shorter wavelengths, at the European XFEL and the Linac Coherent Light Source, will provide a powerful tool that will on one hand give spatial resolutions approaching atomic size and temporal resolutions approaching molecular motion.

7 Conclusions

Coherent x-ray diffraction microscopy is emerging as a powerful tool complimentary to standard x-ray microscopy, electron and light microscopy. The efficiency of CXDM and the achievable resolutions may eventually lead to macro-molecular resolution images of biological structures and near atomic resolution for materials sciences specimens. The ability to image in both phase contrast and absorption contrast simultaneously gives CXDM a further experimental advantage over lens-based imaging systems. These advantages come at a computational cost that limit the throughput of diffraction microscopes. The requirement to optimize up to 1 billion phases, in the case of three-dimensional imaging, requires sophisticated algorithms and state-of-the-art computational resources. Exciting developments in the field of compressive sensing may provide algorithms that can reconstruct images from far fewer Fourier samples than are currently needed [22, 62]. This could provide more reliable imaging from limited experimental data and therefore greatly increase experimental throughput.

CXDM has grown from a single demonstration in 1999 to a vibrant field of research that includes research teams at every third generation synchrotron around the world. With new sources coming online and the upgrade of older sources the available x-ray brightness will lead to many exciting developments and scientific opportunities in the years to come.

8 Acknowledgements

We are very grateful to our colleagues that have granted us permission to reproduce their work in this chapter. In particular we wish to thank Henry Chapman (now at the Center for Free-Electron Laser Science, DESY), John Miao (now at the University of California at Los Angeles), Anton Barty (Lawrence Livermore National Lab), Janos Kirz (Advanced Light Source, Lawrence Berkeley National Lab), Chris Jacobsen (Stony Brook University), Ian Robinson (now at University College, London), David Sayre (Stony Brook University), Pierre Thibault (now at the Paul Scherrer Institute), Malcolm Howells, John Spence (Arizona State University), Enju Lima (now at Brookhaven National Lab), Mark Pfeifer (now at La Trobe University), and Changyong Song (UCLA).

References

- [1] A. N. Skrinsky A. M. Kondratenko. Use of radiation of electron storage rings in x-ray holography of objects. *Opt. Spectrosc.*, 42:189–192, 1977.
- [2] A.C.Schell. *Multiple Plate Antenna*. PhD thesis, Mass. Inst. Tech, 1961.
- [3] David Attwood. *Soft X-Rays and Extreme Ultraviolet Radiation*. Cambridge University Press, 2000.
- [4] R. H. T. Bates. Fourier phase problems are uniquely soluble in more than one dimension. i: underlying theory. *Optik*, 61:247–262, 1982.
- [5] R. H. T. Bates and W. R. Fright. Composite two-dimensional phase-restoration procedure. *J. Opt. Soc. Am.*, 73(3):358, 1983.
- [6] Michael J Bogan, W Henry Benner, Sebastien Boutet, Urs Rohner, Matthias Frank, Anton Barty, M Marvin Seibert, Filipe Maia, Stefano Marchesini, Sasa Bajt, Bruce Woods, Vincent Riot, Stefan P Hau-Riege, Martin Svenda, Erik Marklund, Eberhard Spiller, Janos Hajdu, and Henry N Chapman. Single particle x-ray diffractive imaging. *Nano Lett*, 8(1):310–316, 2008.
- [7] Max Born and Emil Wolf. *Principles of Optics*. Cambridge University Press, 7th edition, 2000.
- [8] Y. M. Bruck and L. G. Sodin. On the ambiguity of the image reconstruction problem. *Optics Communications*, 30(3):304–308, 1979.
- [9] Henry N Chapman, Anton Barty, Stefano Marchesini, Aleksandr Noy, Stefan P Hau-Riege, Congwu Cui, Malcolm R Howells, Rachel Rosen, Haifeng He, John C H Spence, Uwe Weierstall, Tobias Beetz, Chris Jacobsen, and David Shapiro. High-resolution ab initio three-dimensional x-ray diffraction microscopy. *J Opt Soc Am A Opt Image Sci Vis*, 23(5):1179–1200, 2006.
- [10] Henry N Chapman, Stefan P Hau-Riege, Michael J Bogan, Sasa Bajt, Anton Barty, Sebastien Boutet, Stefano Marchesini, Matthias Frank, Bruce W Woods, W Henry Benner, Richard A London, Urs Rohner, Abraham Szoke, Eberhard Spiller, Thomas Moller, Christoph Bostedt, David A Shapiro, Marion Kuhlmann, Rolf Treusch, Elke Plonjes, Florian Burmeister, Magnus Bergh, Carl Caleman, Gosta Huldt, M Marvin Seibert, and Janos Hajdu. Femtosecond time-delay x-ray holography. *Nature*, 448(7154):676–679, 2007.
- [11] Bingquan Chen and Jakob J. Stamnes. Validity of diffraction tomography based on the first born and the first rytov approximations. *Appl. Opt.*, 37(14):2996–3006, 1998.
- [12] E. G. Bessonov D. F. Alferov, Yu. A. Bashmakov. Theory of undulator radiation. *Sov. Phys. Tech. Phys.*, 23:902–904, 1978.
- [13] D.A.Shapiro. *Biological imaging by soft x-ray diffraction microscopy*. PhD thesis, Stony Brook University, 2004.
- [14] D.R.Luke. Relaxed averaged alternating reflections for diffraction imaging. *Inverse Problems*, 21:37:50, 2005.

- [15] D.Sayre. Report on a project on three-dimensional imaging of the biological cell by single-particle x-ray diffraction. *Acta Cryst.*, A64:33–35, 2008.
- [16] D.Starodub. Dose, exposure time and resolution in serial x-ray crystallography. *J.Sync.Rad.*, 15(62-73), 2008.
- [17] S Eisebitt, J Luning, W F Schlotter, M Lorgen, O Hellwig, W Eberhardt, and J Stohr. Lensless imaging of magnetic nanostructures by x-ray spectro-holography. *Nature*, 432(7019):885–888, 2004.
- [18] V Elser. Phase retrieval by iterated projections. *Journal of the Optical Society of America A-Optics Image Science and Vision*, 20:40–55, 2003.
- [19] A.Barty et al. Three-dimensional coherent x-ray diffraction imaging of a ceramic nanofoam: Determination of structural deformation mechanisms. *PRL*, 101:055501, 2008.
- [20] A.Barty et al. Ultrafast single-shot diffraction imaging of nanoscale dynamics. *Nature Photonics*, 2:415, 2008.
- [21] B. Abbey et al. Keyhole coherent diffractive imaging. *Nature Physics*, 4:394–398, 2008.
- [22] M.L.Moravec et al. Compressive phase retrieval. *Wavelets XII. Proc. SPIE*, 6701:670120, 2007.
- [23] M.R.Howells et al. An assessment of the resolution limitation due to radiation damage in x-ray diffraction microscopy. *arXiv:0502059v1*, 2008.
- [24] P.Thibault et al. High-resolution scanning x-ray diffraction microscopy. *Science*, 321(5887):379–382, 2008.
- [25] S. Marchesini et al. Phase aberrations in diffraction microscopy. *IPAP Conf. Series*, 7:380–382, 2006.
- [26] S.P.Hau-Riege et al. Dynamics of x-ray irradiated biological molecules. *Phys.Rev.E*, 69:051906, 2004.
- [27] V. Elser et al. Searching with iterated maps. *Proc. Natl. Acad. Sci. USA*, 104(2):418–423, 2007.
- [28] V.L.Shneerson et al. Crystallography without crystals. i. the common-line method for assembling a three-dimensional diffraction volume from single-particle scattering. *Acta Cryst.*, A64:303–315, 2008.
- [29] M.Cui E.Tang, P.Zhu. Coherence mode of sr. *Acta Optica Sinica*, 18:1645, 1998.
- [30] J. R. Fienup. Reconstruction of an object from the modulus of its fourier transform. *Opt. Lett.*, 3(1):27, 1978.
- [31] J. R. Fienup. Phase retrieval algorithms: a comparison. *Appl. Opt.*, 21(15):2758–2769, 1982.
- [32] J. R. Fienup. Reconstruction of a complex-valued object from the modulus of its fourier transform using a support constraint. *J. Opt. Soc. Am. A*, 4(1):118, 1987.

- [33] J. R. Fienup, T. R. Crimmins, and W. Holsztynski. Reconstruction of the support of an object from the support of its autocorrelation. *J. Opt. Soc. Am.*, 72(5):610, 1982.
- [34] G.J.Williams. Fresnel coherent diffractive imaging. *PRL*, 97:025506, 2006.
- [35] M. H. Hayes and J. H. McClellan. Reducible polynomials in more than one variable. *Proc. IEEE*, 70(2):197–198, 1982.
- [36] B.L. Henke, E.M. Gullikson, and J.C. Davis. X-ray interactions: Photoabsorption, scattering, transmission, and reflection at $e = 50\text{--}30,000$ eV, $z = 1\text{--}92$. *Atomic Data and Nuclear Data Tables*, 54:181, 1993.
- [37] H.N.Chapman. Femtosecond diffractive imaging with a soft-x-ray free-electron laser. *Nature Physics*, 2:839, 2006.
- [38] H.N.Chapman. Focus on x-ray diffraction. *Science*, 321(5887):352–353, 2008.
- [39] I.K.Robinson. Reconstruction of the shapes of gold nanocrystals using coherent x-ray diffraction. *PRL*, 87(19):195505, 2001.
- [40] J.C.H.Spence. Coherence and sampling requirements for diffractive imaging. *Ultramicroscopy*, 101(2-4):149–152, 2004.
- [41] J.Frank. Computer averaging of electron micrographs of 40s ribosomal subunits. *Science*, 214(1353), 1981.
- [42] M.R.Howells J.Kirz, C.J.Jacobsen. Soft x-ray microscopes and their biological applications. *Q.Rev.Biophys.*, 28:33–130, 1995.
- [43] J.M.Rodenburg. *Advances in Imaging and Electron Physics*, volume 150, chapter Ptychography and related diffractive imaging methods. Elsevier, 2008.
- [44] J.W.Goodman. *Statistical Optics*. Wiley, 1985.
- [45] Enju Lima. *The Advancement of Biological Imaging Through X-Ray Diffraction Microscopy*. Ph.d. thesis, Stony Brook University, Nichols Road, Stony Brook, New York 11794-3800, August 2006.
- [46] H. Winick M. Cornacchia. Xv int. conf. on high energy accel. *Science*, 228:1265–1272, 1985.
- [47] Stefano Marchesini. Phase retrieval and saddle-point optimization. *J Opt Soc Am A Opt Image Sci Vis*, 24(10):3289–3296, 2007.
- [48] M.H.Hayes. The reconstruction of a multidimensional sequence from the reconstruction of a multidimensional sequence the phase or magnitude of its fourier transform. *IEEE Trans. ASSP*, 30(2):140–154, 1982.
- [49] J. Miao, P. Charalambous, J. Kirz, and D. Sayre. Extending the methodology of x-ray crystallography to allow imaging of micrometre-sized non-crystalline specimens. *Nature*, 400:342–344, July 1999.

- [50] J. Miao, D. Sayre, and H. N. Chapman. Phase retrieval from the magnitude of the fourier transforms of nonperiodic objects. *J. Opt. Soc. Am. A*, 15(6):1662–1669, 1998.
- [51] Jianwei Miao, Keith O Hodgson, Tetsuya Ishikawa, Carolyn A Larabell, Mark A LeGros, and Yoshinori Nishino. Imaging whole escherichia coli bacteria by using single-particle x-ray diffraction. *Proc Natl Acad Sci U S A*, 100(1):110–112, 2003.
- [52] J. Von Neumann. On rings of operators. reduction theory. *Annals of Mathematics*, 50(2):401–485, 1949.
- [53] Mark A Pfeifer, Garth J Williams, Ivan A Vartanyants, Ross Harder, and Ian K Robinson. Three-dimensional mapping of a deformation field inside a nanocrystal. *Nature*, 442(7098):63–66, 2006.
- [54] Q.Shen. Diffractive imaging of nonperiodic materials with future coherent x-ray sources. *J.Sync.Rad.*, 11:432–438, 2004.
- [55] B Reuter and H Mahr. Experiments with fourier transform holograms using 4.48 nm x-rays. *Journal of Physics E: Scientific Instruments*, 9(9):746–751, 1976.
- [56] R.Neutze. Potential for biomolecular imaging with femtosecond x-ray pulses. *Nature*, 406:752–757, 2000.
- [57] R.W.Gerchberg and W.O.Saxton. A practical algorithm for the determination of phase from image and diffraction plane pictures. *Optik*, 35:237, 1972.
- [58] David Sayre. *Imaging Processes and Coherence in Physics*, page 229. Springer-Verlag, 1980.
- [59] W. F. Schlotter, R. Rick, K. Chen, A. Scherz, J. Stoehr, J. Luening, S. Eisebitt, Ch. Guenther, W. Eberhardt, O. Hellwig, and I. McNulty. Multiple reference fourier transform holography with soft x rays. *Applied Physics Letters*, 89, 2006.
- [60] DA Shapiro. Report on a project on three-dimensional imaging of the biological cell by single-particle x-ray diffraction. addendum. *Acta Crystallogr A*, 64(Pt 1):36–37, 2008.
- [61] David Shapiro, Pierre Thibault, Tobias Beetz, Veit Elser, Malcolm Howells, Chris Jacobsen, Janos Kirz, Enju Lima, Huijie Miao, Aaron M Neiman, and David Sayre. Biological imaging by soft x-ray diffraction microscopy. *Proc Natl Acad Sci U S A*, 102(43):15343–15346, 2005.
- [62] S.Marchesini. Ab initio compressive phase retrieval. *JOSA submitted*, arXiv:0809.2006, 2008.
- [63] Changyong Song, Raymond Bergstrom, Damien Ramunno-Johnson, Huaidong Jiang, David Paterson, Martin D de Jonge, Ian McNulty, Jooyoung Lee, Kang L Wang, and Jianwei Miao. Nanoscale imaging of buried structures with elemental specificity using resonant x-ray diffraction microscopy. *Phys Rev Lett*, 100(2):025504, 2008.
- [64] Pierre Thibault, Veit Elser, Chris Jacobsen, David Shapiro, and David Sayre. Reconstruction of a yeast cell from x-ray diffraction data. *Acta Crystallogr A*, 62(Pt 4):248–261, 2006.
- [65] W.Hoppe. Diffraction in inhomogeneous primary wave fields. 1. principle of phase determination from electron diffraction interference. *Acta Cryst.*, A25(495-501), 1969.

- [66] W.Hoppe. Diffraction in inhomogeneous primary wave fields. 3. amplitude and phase determination for nonperiodic objects. *Acta Cryst.*, A25:508–515, 1969.
- [67] Z.Jurek. Dynamics in a cluster under the influence of intense femtosecond hard x-ray pulses. *Eur.Phys.J*, D29:217–229, 2004.